Jet production in deep inelastic scattering at small Bjorken x

Master's thesis, 25.5.2021

Author:

Laura Huhta

Supervisor:

Heikki Mäntysaari

JYVÄSKYLÄN YLIOPISTO
FYSIIKAN LAITOS

Abstract

Huhta, Laura
Jet production in deep inelastic scattering at small Bjorken x
Master's thesis
Department of Physics, University of Jyväskylä, 2021, 58 pages.

High energy collisions enable studies of very dense systems of gluons, which lead to a type of matter known as color glass condensate (CGC). In this gluon saturation regime, non-linear effects such as gluon recombination become important. Clear observations of saturated gluonic matter have not yet been achieved, therefore these observations are a major goal of future collider experiments such as the Electron-Ion Collider (EIC) at Brookhaven National Laboratory (BNL).

In this thesis, we study jet production in the virtual photon-proton (γ^*-p) and virtual photon-nucleus (γ^*-A) subprocesses of deep inelastic scattering (DIS) in the dipole picture. We find that the jet production cross section in γ^*-A processes is suppressed at small x when compared to the scaled γ^*-p cross section. This suppression results from enhanced non-linear dynamics in heavy nuclei as compared to the proton. The nuclear suppression is found to depend on photon polarization. Also, nuclear enhancement known as the Cronin effect is observed at Bjorken $x \approx 10^{-2}$ and is seen to diminish with decreasing x, suggesting enhancement to be visible at the EIC at a specific kinematic range. Two MV model based parametrizations used to calculate initial conditions for the small-x evolutions of the dipole amplitudes are compared and a slight difference between the models is seen. This suggests that EIC data could be used to constrain the dipole amplitude towards a best-suited model.

Keywords: jet production, gluon saturation, dipole picture, deep inelastic scattering

Tiivistelmä

Huhta, Laura
Jettituotto syvässä epäelastisessa sironnassa pienen Bjorken x:n alueessa
Pro gradu -tutkielma
Fysiikan laitos, Jyväskylän yliopisto, 2021, 58 sivua

Korkeaenergiset törmäykset mahdollistavat tutkimuksen hyvin tiheissä gluonisysteemeissä, joissa aine on värilasikondensaatiksi (CGC) kutsutussa olomuodossa. Tällaisessa tiheän gluoniaineen alueessa epälineaariset ilmiöt kuten gluonirekombinaatio ovat merkittäviä. Saturoituneesta gluonisesta aineesta ei olla vielä tehty varmoja havaintoja, ja tämä onkin tulevien kiihdytinkokeiden, kuten Brookhavenin kansalliseen laboratorioon (BNL) rakennettavan Elektroni-ionikiihdyttimen (EIC), yksi päätavoitteista.

Tässä työssä tutkitaan dipolikuvassa jettituottoa prosesseissa, joissa virtuaalinen fotoni siroaa protonista (γ^*-p) tai ytimestä (γ^*-A), ja jotka ovat syvän epäelastisen sironnan (DIS) aliprosesseja. Huomataan, että pienessä x:n alueessa jettituottovaikutusala γ^*-A-prosesseissa kokee suppressiota verrattuna skaalattuun γ^*-p-vaikutusalaan. Tämä ydinsuppressio johtuu lisääntyneestä epälineaarisesta dynamiikasta raskaissa ytimissä verrattuna protoniin. Työssä nähdään, että ydinsuppressio riippuu fotonin polarisaatiosta. Lisäksi alueessa, jossa Bjorken $x \approx 10^{-2}$, havaitaan Cronin-ilmiö, jolloin suppression sijaan γ^*-A-prosessin jettituotto kasvaa suhteessa γ^*-p-prosessiin. Ilmiö heikentyy ja lopulta katoaa kun x pienenee. Tämän pohjalta voidaan odottaa, että EIC:ssä havaittaisiin Cronin-ilmiötä tietyllä kinemaattisella alueella. Työssä verrataan kahta eri parametrisaatiota MV-mallille, jota käytetään dipoliamplitudien laskemisessa, ja niiden välillä nähdään pientä eroavaisuutta. Jettituottomittaukset EIC:ssä voivat siis edistää sopivan dipoliamplitudimallin määrittämistä.

Avainsanat: jettituotto, gluonisaturaatio, dipolikuva, syvä epäelastinen sironta

Contents

1 Introduction

Quantum chromodynamics (QCD) is the theory of strong interactions, describing the behavior of quark and gluon fields. The theory of QCD was first formulated in the 1970's, and today it is considered one of the cornerstones of our Standard Model. High energy collisions are abundant with QCD effects, some of which cannot be detected in lower energy experiments. An especially interesting area of study in this high energy regime has been that of very dense systems of quarks and gluons, in which the coupling constant is small. When we observe the partons in a hadron at high energy, we see an increase in the gluon density of the nucleus, due to gluon splitting. However, at some point a limit to the growth, a saturation point, has to be reached. This occurs when the gluon density is high enough for gluon recombination, a nonlinear process, to become just as relevant as the process of gluon splitting. These nonlinear dynamics have been theorized to be visible at high gluon densities, which is equivalent to small momentum fraction x, as data from HERA has shown. [1]

In this thesis, we focus on deep inelastic scattering (DIS), a process which enables the probing of hadron constituents, much like Rutherford's gold foil experiments probed the nuclear structure of atoms. A benefit of studying DIS is that the projectile lepton has no substructure, so that when the scattered lepton is measured, we can obtain all information on the kinematics of the event. This cannot be done, for example, in proton-proton collisions, in which the momenta of all the constituent partons are unknown. DIS measurements are of great historical significance as they led physicists to first clear evidence of the internal structure of hadronic matter. Experiments performed at the Hadron-Electron Ring Accelerator (HERA) at the Deutsches Elektronen-Synchrotron (DESY) have provided very precise measurements of the internal structure of the proton by colliding electrons and positrons with protons. [1] The accelerator experiment finished its measurements in 2007, and, after that, data for the study of QCD dynamics has been provided by particle accelerators such as the Relativistic Heavy Ion Collider (RHIC) at Brookhaven National Laboratory (BNL) and the Large Hadron Collider (LHC) at CERN.

While existing accelerator experiments continue to provide important data for QCD studies, new experiments are needed to investigate the field further. As previ-

ous experiments have not yet been successful in clearly observing nonlinear effects in nuclei, their study will be a major goal in some upcoming future collider experiments. These include the Electron-Ion Collider (EIC) [2] planned to be built at BNL and the Large Hadron-electron Collider (LHeC) [3] to be built at CERN, both admitting a wide range of kinematics, high luminosities, high energies and, at the EIC, polarized beams. These experiments are expected to provide important data in the areas of gluon saturation, the dense gluon matter known as color glass condensate (CGC), parton distibution in hadrons and confinement physics.

Our goal in this work is to calculate the cross sections for jet production in DIS involving photons and both target protons and gold nuclei. This will allow us to calculate nuclear suppression ratios, which provide a way to study how nonlinear QCD dynamics affect the partonic structure of a nucleus at high energy. We consider semi-inclusive DIS processes, because by this we do not limit the final product as much as in exclusive processes, but instead consider any final hadronic states along with a quark (jet) with some specific transverse momentum. The kinematic region and the interacting hadrons (protons and gold nuclei) chosen for our study have been chosen with the EIC in mind, as these kinematic ranges and specific target hadrons will be utilized in the experiment. By comparing two different parametrization models for the initial condition input of the Balitsky-Kovchegov (BK) evolution equation, we also aim to study the model uncertainty of our jet production cross sections.

The structure of this thesis is as follows. First, in Chapter 2, we will present the basic kinematics of the DIS process as well as the dipole model, and discuss gluon saturation effects. After that, in Chapter 3, we present an analytic calculation of the cross sections for inclusive one- and two-jet production in photon-proton and photon-nucleus interactions. The photon-proton cross section calculation closely follows that done in Ref. [4] for exclusive processes. In Chapter 4, we consider future experimental setups which are designed to study DIS and gluon saturation at wider kinematical ranges than have yet been possible. Finally, in Chapter 5, we present the results of our numerical calculations, including cross sections and nuclear suppression ratios for varying kinematic ranges. Also, by comparing two different parametrization models we make a quantified approximation of the model uncertainty of our results.

On units and notation: In this thesis, we adopt the commonly used system of natural units. This means that the speed of light, the reduced Planck's constant

and the Boltzmann constant are equated to unity: $c = \hbar = k_B = 1$. This allows us to conveniently work in the following units:

$$[\text{mass}] = [\text{length}]^{-1} = [\text{time}]^{-1} = [\text{energy}] = \text{GeV}. \tag{1}$$

We use **bold** font to refer to a 2D vector, while plain font is used to refer to four-vectors. We will utilize the light cone coordinate system, which means that in addition to the usual four-component vectors $x = (x^0, x^1, x^2, x^3)$, we will also use vectors of the form $x = (x^+, x^-, \mathbf{x}_\perp)$. The components of these vectors are defined here as

$$x^\pm = \frac{1}{\sqrt{2}}(x^0 \pm x^3),\ (\mathbf{x}_\perp)^1 = x^1,\ (\mathbf{x}_\perp)^2 = x^2, \tag{2}$$

where we refer to the x^+ coordinate as the light cone time coordinate. (One could just as well choose the x^- coordinate as the time coordinate.) The normalization of the light cone vectors can differ depending on the reference used. [5] The metric tensor $g^{\mu\nu}$ for light cone coordinates has the non-zero elements

$$g^{+-} = g^{-+} = 1,\ g^{11} = g^{22} = -1. \tag{3}$$

The dot product of two vectors in the light cone coordinates, a and b, thus gives

$$a \cdot b = a^\mu b_\mu = a^+ b^- + a^- b^+ - \mathbf{a}_\perp \cdot \mathbf{b}_\perp. \tag{4}$$

2 Deep inelastic scattering at high energy

2.1 Deep inelastic scattering

Deep inelastic scattering (DIS) is a lepton-hadron scattering process that provides a way to probe the insides of hadrons as well as enables the testing of the theory of perturbative quantum chromodynamics (pQCD). The first DIS experiments able to probe the constituent substructure of hadrons were carried out at the Stanford Linear Accelerator Center (SLAC) in 1968, and it was these experiments which led physicists to first clear evidence of pointlike partons we now know as quarks. Today, DIS processes are studied to provide precise tests of perturbative QCD theory such as determining momentum distributions of partons in hadrons in order to predict cross sections in high energy hadron collisions. [6]

The DIS process of a lepton scattering from a hadron is dominated by the exchange of a virtual photon, with small corrections arising from multiphoton exchanges. Also, instead of an exchanged photon, the exchange of a Z^0 boson is a possibility in these interactions, this exchange becoming relevant at values of virtuality $Q^2 \sim M_Z^2$, where $-Q^2$ is the squared four-momentum transfer and M_Z is the mass of the Z^0 boson. The exchanged photon acts as a probe of the proton structure, and this ability to probe tiny structures is the reason why the scattering is referred to as deep. In order to probe the smallest constituents of the hadron and resolve individual quarks, the photon exchanged in the DIS process requires a large virtuality Q^2, which in turn corresponds to the photon's wavelength being very small, as compared to the size of the hadron. The emission of a photon from a lepton is a well-known phenomenon which can be calculated using quantum electrodynamics (QED), while the photon-hadron interaction is a more complicated process. Therefore, while experimentally DIS is studied by colliding leptons and hadrons, we focus our study on the interaction between the exchanged virtual photon and the target hadron.

Considering the scattering of a high-energy charged lepton off a hadron target in a target rest frame (TRF), such as in Fig. 1, we label the incoming and outgoing lepton four-momenta by k^μ and k'^μ, respectively. The momentum of the target

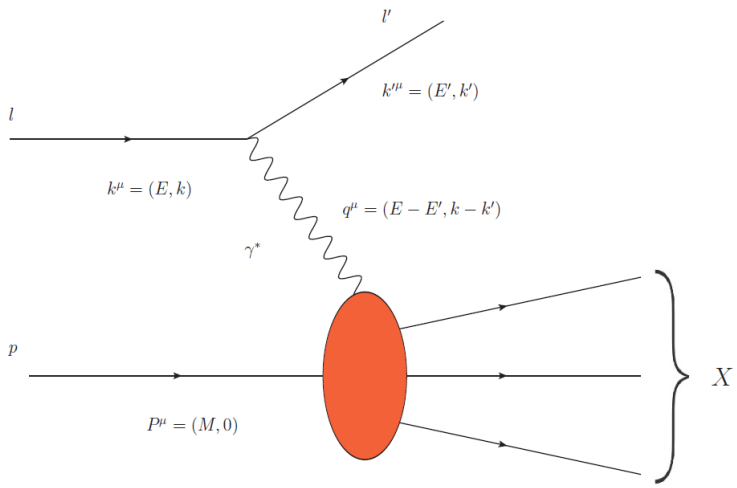

Figure 1. A Feynman diagram of deep inelastic scattering between an initial lepton l and a target proton p in the rest frame of the proton. The scattering is mediated by a virtual photon.

hadron is labeled P^{μ} and the momentum transfer $q^{\mu} = k^{\mu} - k'^{\mu}$. We can write this process as $l(k) + p(P) \rightarrow l(k') + X(P_X)$, where we have chosen the target to be a proton, p, and where X signifies any hadronized final state of momentum P_X. The standard, Lorentz invariant deep inelastic variables for a target proton are defined as follows: [6]

$$\begin{aligned} Q^2 \equiv -q^2 = -(k - k')^2, \qquad & 2M\nu = W^2 + Q^2 - M^2, \\ W^2 = (P + q)^2, \qquad & x \equiv \frac{Q^2}{2P \cdot q} = \frac{Q^2}{2M\nu}, \end{aligned} \tag{5}$$

where the dimensionless variable x is the Bjorken scaling variable, $M^2 = P^2$ signifies the target mass squared, $\nu \equiv (P \cdot q)/M$ and W^2 is the squared invariant mass of the hadron state X. In the case of virtual photons, which are off-shell, the photon virtuality Q^2 is non-zero. In the rest frame of the target, $\nu = E - E'$, where E, E' are the energies of the incoming and outgoing leptons, and therefore in this frame ν can be regarded as a Lorentz invariant generalization for energy transfer from the lepton to the proton.

In the target rest frame, the model of the target hadron consisting of partons is not applicable. In order to develop a parton model picture of DIS, in which the target hadron is composed of valence quarks, sea quarks and gluons, we consider an infinite

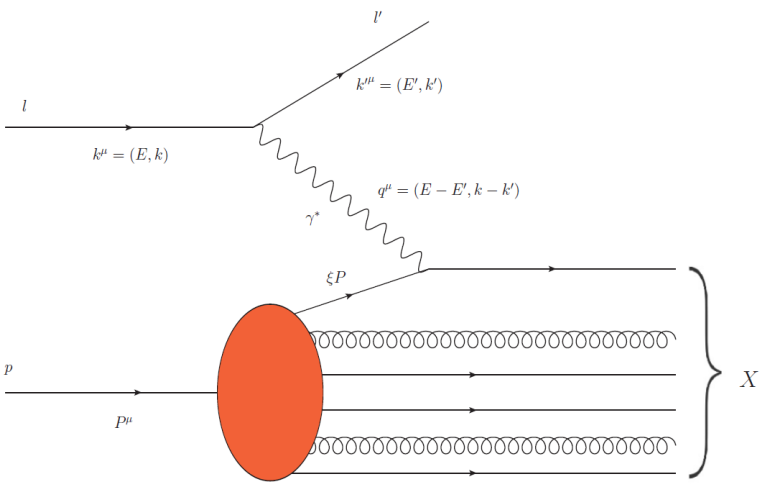

Figure 2. A Feynman diagram of deep inelastic scattering between an initial lepton l and a target proton p in the infinite momentum frame (IMF). The parton model is valid in the IMF, and the constituent quarks and gluons of the proton are pictured.

momentum frame (IMF) in which the proton moves very fast in the z-direction, $P^{\mu} \approx (P, 0, 0, P)$, with $P \gg M$. In the IMF, we can view the target proton as a stream of partons moving parallel with the proton, with each individual parton carrying a fraction ξ of the proton's momentum, see Fig. 2. In this frame, for large Q^2, inelastic scattering is dominated by two-step processes: the first step is an elastic scattering of a lepton off a quark in the proton, and the second step is a fragmentation process which converts the recoil quark and the rest of the remaining proton constituents into hadrons, denoted by X. For $Q^2 \gg M^2$, the fraction of proton momentum, ξ, carried by the struck parton is equal to Bjorken x. An important benefit of working in an infinite momentum frame is that the time taken for the DIS process to occur is much shorter than the time required for any internal processes to take place inside the target hadron. [6]

If we consider the target proton or nucleus in the IMF at small x, at very high energies, we see the target becoming highly Lorentz contracted in the direction of motion, forming a thin "pancake". In this regime, the target is expected to mostly consist of small-x, soft, gluons, as small values of x have been shown to correlate with high gluon densities in HERA structure function measurements [1]. The high density of soft gluons enables us to treat the target as a color field. This type of matter is called the color glass condensate (CGC), which we discuss further in Sec.

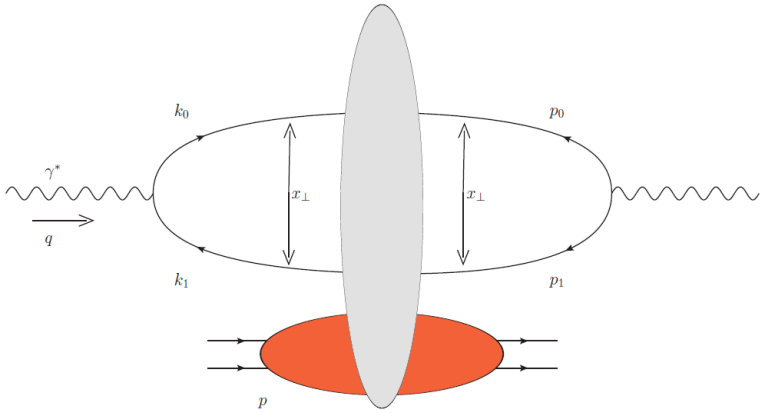

Figure 3. The forward scattering amplitude for DIS in TRF. The virtual photon first splits into a quark-antiquark dipole, which then interacts with the proton (red). The interaction is symbolized by the grey oval. The constant transverse position of the quarks is indicated with $x_\perp$.

2.3.

We now consider the scattering of a virtual photon from this CGC color field, in a frame where the target momentum is low. The photon can split into a color charged quark-antiquark pair, remain as a photon or split into a lepton pair. However, only the quark-antiquark pair can interact with the color field via strong interaction, while the photon and the lepton pair cannot. This leads us to the dipole picture of DIS, where the dominant process is that of a virtual photon fluctuating into a color-neutral quark-antiquark pair, which then interacts with the color field of the target hadron. The forward scattering amplitude for the DIS process in the dipole model is pictured in Fig. 3. By the optical theorem, calculating the imaginary part of the forward scattering amplitude gives us the total cross section for the scattering.

For the dipole picture to be valid, the lifetime of the dipole fluctuation must be longer than the time of interaction with the proton. This can be shown by considering the coherence length of the virtual photon into the longitudinal plus direction, $x^+ \approx 2q^+/Q^2$, and noticing that this is much larger than the size of the nucleus. [5] Therefore, when the virtual photon fluctuates into a $q\bar{q}$ pair, the typical lifetime of the fluctuation is much longer than the nuclear diameter. Thus, the virtual photon has time to first fluctuate into a dipole, which can then interact with the target.

Because we consider scattering at high energy, we can approximate the transverse

positions of the partons to be constant as they interact with the target, due to their transverse momentum being much smaller than the momentum in the direction of motion. This is known as the eikonal approximation, and this approximation can be justified by noticing that, while traversing through the target, the transverse distance $x_\perp$ between the quark and antiquark can only vary by an amount [5]

$$\Delta x_\perp \approx R\frac{k_\perp}{E}. \tag{6}$$

Here, E is the dipole energy in target rest frame, R is the longitudinal size of the target and $k_\perp$ is the relative transverse momentum of the $q\bar{q}$ pair obtained from the scattering. We can recognise the term $k_\perp/E$ as the relative transverse velocity of the quark with respect to the antiquark, and multiplying this by the longitudinal size of the target gives us an approximation of the change in the transverse separation of the dipole. From Eq. (6), we can see that at large energies, and therefore at small x, the change in dipole size is very small. Because the size of the dipole effectively does not change during high-energy scattering, working in transverse coordinate space is a common and convenient choice when calculating DIS cross sections. [5]

2.2 Kinematics

Generally, inclusive DIS considers processes with any possible final states. In this thesis, we are interested in a final product of one or two quarks (experimentally measured as particles or jets) of some specific transverse momentum along with other final hadrons of any type. This type of process where a specific hadron as well as the scattered lepton are detected is known as semi-inclusive DIS (SIDIS). In semi-inclusive DIS, the longitudinal momentum taken from the target is marked by x_p. To express this in terms of the Bjorken x and other kinematical factors, we consider the initial proton and photon momenta, P^μ and q^μ, in the previously described light cone coordinates:

$$\begin{aligned} P^\mu &= \left(\frac{m_p^2}{2P^-}, P^-, \mathbf{0}\right), \\ q^\mu &= \left(q^+, \frac{-Q^2}{2q^+}, \mathbf{0}\right). \end{aligned} \tag{7}$$

The frame here has been chosen such that the proton and photon have no transverse momentum. Also, as we are now focused on high energy processes, we consider the

high energy limit where q^+ and P^- are both large. Now, for the total photon-proton scattering energy W we have

$$W^2 = (P+q)^2 \approx 2(P\cdot q) \approx 2P^- q^+, \tag{8}$$

where the first approximation is that both $P^2 = m_p^2$ and q^2 are much smaller than the total energy W of the process, and the second approximation is that q^+ and P^- are much larger than q^- and P^+.

We require the dipole, represented by the four-vector p^μ, to be on-shell so that $p^2 = M_{q\bar{q}}^2$, where $M_{q\bar{q}}$ is the invariant mass of the quark-antiquark dipole. From this and Eq. (4), since the dipole has no transverse momentum, we obtain

$$p^- = \frac{M_{q\bar{q}}^2}{2p^+}. \tag{9}$$

We know that both + and − components of momentum are separately conserved in the process and that x_p is the fraction of momentum taken from the target, thus, momentum conservation and Eq. (9) lead to

$$\begin{aligned} q^- + P^- &= (1-x_p)P^- + p^- \\ &= (1-x_p)P^- + \frac{M_{q\bar{q}}^2}{2p^+}, \end{aligned} \tag{10}$$

and therefore we have for x_p that

$$x_p = \frac{M_{q\bar{q}}^2}{2p^+P^-} - \frac{q^-}{P^-}. \tag{11}$$

Using this and Eq. (7) we can express x_p as

$$x_p = \frac{M_{q\bar{q}}^2}{2p^+P^-} - \frac{-Q^2}{2P^-q^+} \approx \frac{M_{q\bar{q}}^2}{W^2} + \frac{Q^2}{W^2}, \tag{12}$$

where in the final step we use the fact that $q^+ = p^+$ as well as our earlier approximation (8) for W^2. So, finally, we have for the fraction of longitudinal momentum taken from the target

$$x_p \approx \frac{Q^2 + M_{q\bar{q}}^2}{W^2} \approx x + \frac{M_{q\bar{q}}^2}{W^2}, \tag{13}$$

where x is the Bjorken x variable defined in Eq. (5) and where we have assumed $W^2 \gg Q^2, M^2$.

We define the longitudinal momentum fraction z_i $(i = 0, 1)$ for the quark and antiquark with respect to the virtual photon as $z_i \equiv \frac{k_i^+}{q^+}$, where q^+ denotes the light cone longitudinal momentum of the incoming photon and k_i^+ that of the quark or antiquark before interaction. The invariant mass of the dipole pair, $M_{q\bar{q}}^2$, can be expressed in terms of this momentum fraction z_i and the initial momenta k_i of the quarks, which becomes useful when comparing calculations to experimental results. We can write the momenta k_i of the quarks in light cone coordinates as $k_i = (k_i^+, k_i^-, \mathbf{k}_{i\perp})$, and we know that k_i^+ is large, since q^+ is large. Furthermore, we work at a scale of large energies which allows us to ignore the mass term, so that finally we have, writing $k_i^+ = q^+ z_i$, that $k_i^- = \mathbf{k}_{i\perp}^2/(2q^+ z_i)$.

Now, we can calculate for the invariant mass,

$$\begin{aligned} M_{q\bar{q}}^2 &= (k_0 + k_1)^2 = 2k_0 \cdot k_1 = 2\left(k_0^+ k_1^- + k_0^- k_1^+ - \mathbf{k}_{0\perp} \cdot \mathbf{k}_{1\perp}\right) \\ &= 2\Big(\frac{\mathbf{k}_{1\perp}^2 z_0}{2z_1} + \frac{\mathbf{k}_{0\perp}^2 z_1}{2z_0} - \mathbf{k}_{0\perp} \cdot \mathbf{k}_{1\perp}\Big) \\ &= \mathbf{k}_{0\perp}^2 \left(1 + \frac{z_1}{z_0}\right) + \mathbf{k}_{1\perp}^2 \left(1 + \frac{z_0}{z_1}\right) - (\mathbf{k}_{0\perp} + \mathbf{k}_{1\perp})^2 . \end{aligned} \tag{14}$$

Finally, we get the following form for the invariant mass of the dipole,

$$M_{q\bar{q}}^2 = \frac{\mathbf{k}_{0\perp}^2}{z_0} + \frac{\mathbf{k}_{1\perp}^2}{z_1} - (\mathbf{k}_{0\perp} + \mathbf{k}_{1\perp})^2 . \tag{15}$$

The final term in Eq. (15) is equal to zero before scattering as the quarks are back-to-back, and even after interacting with the target the term is presumed to be smaller than the two other terms. Also, it should be noted that, in this thesis, the other of the quarks is integrated over in order to let its final state be undetermined when we study one-jet production.

Another useful variable when considering experimental results is particle rapidity y. Experimentally, one can measure rapidity as well as the center-of-mass energy squared W^2. Therefore, it is useful for us to express the momentum fraction z_i as a function of these variables. We know that for massless particles, the energy, E, and the z component of momentum, k_z, are [7]

$$E = k_T \cosh(y), \qquad\qquad k_z = k_T \sinh(y). \tag{16}$$

We can then express the momentum fraction z_i as

$$\begin{aligned} z_i &= \frac{k_i^+}{q^+} = \frac{1}{\sqrt{2}q^+}(k_i^0 + k_i^3) = \frac{1}{\sqrt{2}q^+}k_{iT}(\cosh y_i + \sinh y_i) \\ &= \frac{1}{\sqrt{2}q^+}k_{iT}e^{y_i} = \frac{2E_p k_{iT}}{W^2}e^{y_i}, \end{aligned} \tag{17}$$

where in the final equality we have used the fact that $W^2 \approx 2P^-q^+ = 2\sqrt{2}E_p q^+$, where E_p is the energy of the target. Thus, we have expressed z_i as a function of particle rapidity y_i, target energy E_p, and particle transverse momentum k_{iT}, all experimentally measurable quantities.

2.3 Gluon saturation

Since at high energy we have a large value for the center-of-mass energy W of the photon-nucleon system, then, according to Eqs. (5) and (13), the value of x is small. We know from studies performed at small values of x that gluon densities in protons appear to grow as x decreases. This has been shown most notably in the H1 and ZEUS experiments conducted at HERA, where precision measurements of the proton structure functions were performed. [1] From these, through QCD analysis, the parton distribution functions could then be determined.

When its virtuality Q^2 is increased, the virtual DIS photon starts to see a larger amount of sea quarks and antiquarks, which originate from gluon splitting ($g \to q\bar{q}$), suggesting a larger amount of gluons present as well. The evolution of gluon density with Q^2 is described by the Dokshitzer-Gribov-Lipatov-Altarelli-Parisi (DGLAP) evolution equations. [8–11] With decreasing x and at a fixed scale Q^2, gluon splitting processes ($g \to gg$) increase the gluon density at a rate which is linearly proportional to gluon density ρ. In this linear regime, at relatively low gluon densities the Balitsky-Fadin-Kuraev-Lipatov (BFKL) equation [12, 13] predicts the gluon splitting mechanism to fill up the space in the hadron with small momentum fraction gluons. [14] At higher densities, the gluons in the hadron begin to overlap with each other as more and more of them are formed via splitting. At a high enough density, gluon fusion ($gg \to g$) effects become relevant, as this fusion is proportional to ρ^2. At a certain point, the effect of this nonlinear gluon fusion process becomes enough to compensate for the gluon splitting and a point of saturation is reached at a saturation scale Q_s. At gluon transverse momenta lower than this scale, saturation effects are noticeable.

In this work, we consider protons and heavy nuclei of mass number A as our target hadrons. We know that, at high energies, the Lorentz contraction of the nucleus causes there to be $\sim A^{1/3}$ overlapping nucleons. This means that if we probe both a heavy nucleus and a proton, we should see nonlinear effects caused by gluon fusion taking place already at larger x_p in the nucleus than in the proton. This is to say that the saturation scale Q_s of the nucleus is larger than that of the proton when both are probed at the same x_p.

At the saturation scale, the dilute, unsaturated, confined quarks and gluons in the hadron are separated from the saturated soft gluon matter. This type of matter state is referred to as the color glass condensate (CGC) [15], which is based on a classical effective theory formulated by McLerran and Venugopalan [16–18]. In the CGC picture, the number of soft gluons in the target at small x_p is in fact so large that the target hadron can as well be described using classical gluon fields rather than Fock states with a finite amount of gluons. [19] The fast partons in the hadron, such as the valence quarks, are treated as sources for these classical color fields, which represent the soft, small-x gluons in the hadron. [15]

At the limit of an infinite boost, the target field can be considered a shock wave field due to Lorentz contraction. Now, when the incoming virtual photon interacts infinitely fast with the infinitely thin target shock wave color field, the transverse position of partons stays the same and only an eikonal phase is picked up by the incoming photon wave function. [4] This eikonal phase can be described by a quantity known as a Wilson line [20]. Wilson lines serve the purpose of acting as the relevant degrees of freedom for high-energy scattering. [21]

Generally, the Wilson line in the fundamental representation is the path-ordered exponential of a gauge field along a line,

$$U_F = P \exp\Big(ig \int_C A_\mu \mathrm{d}z^\mu \Big), \tag{18}$$

where P denotes path-ordering of the operators in the integral, C is an arbitrary (not necessarily closed) contour, and $A_\mu = \sum_a t^a A_\mu^a$ is a gauge field, where the t^a are the SU(3) generators in the fundamental representation. [22] In this work, we have the integration variable z such that the integration bounds are from $z = -\infty$ to $z = \infty$, A_μ is the gluon field of the target, we choose a light cone gauge such that $A^+ = 0$, and we set $x^- = 0$ since we can approximate the particle to propagate

along x^+. From these, we get a form for the Wilson line such that [5]

$$U_F(\mathbf{x}_\perp) = P \exp\left(ig \int_{-\infty}^{\infty} A^-(z^+, \mathbf{x}_\perp) \mathrm{d}z^+\right). \tag{19}$$

When a quark, represented by the state $|q_\alpha\rangle$ where α denotes the color index of the quark before interaction, scatters off a target, or rather, propagates through the dense gluon field at fixed transverse position, it gains a phase which is represented by a Wilson line. This can be written as [4]

$$|q_\alpha\rangle \xrightarrow{\text{scattering}} U_{F\alpha\beta} |q_\beta\rangle , \tag{20}$$

where β represents the color index of the quark after the scattering. The process is similar for antiquark states, with the only difference being that the Wilson line is replaced by its Hermitian conjugate $U^\dagger_{F\beta\alpha}$. In our calculations, the dipole amplitude $\mathcal{N}$ can be defined using these Wilson lines, as

$$\mathcal{N}_{01} = 1 - \mathrm{Tr}\left(U_F(\mathbf{x}_0) U_F^\dagger(\mathbf{x}_1)\right). \tag{21}$$

Gluon fusion is a necessary mechanism to limit the gluon density growth. If the density was allowed to grow indefinitely, the cross section for DIS processes would also grow indefinitely and this would violate the Froissart bound, a consequence of the unitarity of the S-matrix which states a strict, well-established upper limit behavior for the growth of cross sections. [14] In order to limit the linear evolution of the gluons, a nonlinear evolution equation, such as the Balitsky-Kovchegov (BK) equation, is needed. [23, 24] The BK equation describes the energy or Bjorken x dependence of the dipole scattering amplitude. While the BK equation is nonlinear in the saturation regime, it can be reduced to the linear BFKL equation when the nonlinear term is disregarded. The BK equation is only valid for QCD in the large-N_c limit, however, a generalization of the BK equation known as the Jalilian-Marian-Iancu-McLerran-Weigert-Leonidov-Kovner (JIMWLK) equation is valid beyond this limit. [15, 25–28] The JIMWLK equation describes the rapidity or x evolution of the probability distribution of the Wilson lines.

Higher order corrections have been determined for the BK-JIMWLK equations, however, they prove to be of a complicated structure and are very difficult to implement numerically. It has been shown that if we solely consider running coupling corrections to the BK equation, we have an equation which describes most of the

Model	Q_{s0}^2 [GeV^2]	Q_s^2 [GeV^2]	C^2	e_c	$\sigma_0/2$ [mb]
MV	0.104	0.139	14.5	1	18.81
MV^e	0.060	0.238	7.2	18.9	16.36

Table 1. Parameters from fits to HERA data for two different initial condition models, for data at $x < 0.01$ and $Q^2 < 50$ GeV^2. The parameters in this table are from Ref. [34].

higher order effects. [29–31] This running coupling BK equation (rcBK) has been shown to successfully describe data from multiple experiments including data on single [32] and double inclusive [33] spectra in p-p and d-Au collisions at RHIC, where saturation effects are theorized to play a large role.

The rcBK equation requires an input dipole amplitude at an initial x, here chosen to be $x_0 = 0.01$, and the dipole amplitudes at $x < x_0$ are then obtained as solutions of the rcBK evolution equation. As an input of the rcBK equation in photon-proton cross sections in Ref. [34], the parametrization of the dipole amplitude $\mathcal{N}^p$ is based on the McLerran-Venugopalan model [35]:

$$\mathcal{N}^p(\mathbf{r}, x = x_0) = 1 - \exp\left[\frac{\mathbf{r}^2 Q_{s0}^2}{4} \ln\left(\frac{1}{|\mathbf{r}|\Lambda_{\mathrm{QCD}}} + e_c \cdot e\right)\right]. \tag{22}$$

The parameter Q_{s0} controls the saturation scale at x_0, and e_c is a factor added to allow the constant inside the logarithm (which works as an infrared cutoff) to differ from e. Also required for the running coupling BK equation is the strong coupling constant α as a function of the transverse separation $|\mathbf{r}| = r$. A form of the function used in Refs. [29] and [34] is

$$\alpha_s(r) = \frac{12\pi}{(33 - 2N_f) \log\left(\frac{4C^2}{r^2 \Lambda_{\mathrm{QCD}}^2}\right)}, \tag{23}$$

where C^2 is an additional fit parameter included to obtain an evolution compatible with data.

The model parameters have been determined by performing a fit to the HERA structure function data at small x, resulting in different parametrization models depending on initial conditions. [29, 34] We use the model MV^e in most of this thesis, where e_c is left as a free parameter for the fitting. We also make a comparison between results given by MV^e and MV models where, in the latter, e_c is set to unity before fitting. The parameters for the two different models are listed in Table 1.

Also listed is the saturation scale, Q_s^2, which can be calculated as the solution of $\mathcal{N}(\mathbf{r}^2 = 2/Q_s^2) = 1 - e^{-1/2}$. Also, the values of the transverse area of the proton, $\sigma_0/2$, are listed, obtained by similar fitting as the other parameters. The value of Λ_{QCD} has been fixed to 0.241 GeV. In this work, the quark mass is set to $m = 0.14$ GeV, and only the three lightest quarks are considered.

3 Cross sections

3.1 Photon-proton cross sections

The process considered in this section is that of a virtual photon γ^* splitting into a quark q and antiquark $\bar{q}$, as per the dipole picture discussed in Sec. 2.1, which then interact with a proton p (or nucleus A). The process results in a final quark q and antiquark $\bar{q}$ along with any combination of hadrons X, written as $\gamma^* + p(A) \to q + \bar{q} + X$. The leading order diagram of the dipole splitting and interaction process is illustrated in Fig. 4. Our goal is to obtain an expression for the inclusive cross section of a single jet, which in this calculation corresponds to one of the quarks in the dipole. To do this, we first find an expression for the inclusive dijet cross section, and subsequently obtain an expression for the single jet case by integrating over the other quark's momentum. We follow similar steps in our calculations as those performed in Ref. [4], where cross sections were calculated for exclusive dijet processes in which the target proton stayed intact.

The first step in calculating the cross sections is to form the state of the virtual photon, for both longitudinally and transversely polarized photons. We can write the state of the incoming virtual photon in the mixed space representation at leading order as [4]

$$|\gamma^*\rangle = \sum_{q\bar{q}\text{ states}} \delta_{\alpha_0\alpha_1}\Psi(z_0, z_1, \mathbf{x_0}, \mathbf{x_1})\,|q_{\alpha_0}\bar{q}_{\alpha_1}\rangle_{\text{mixed}}\,. \tag{24}$$

The longitudinal momentum fraction of the quark and antiquark are denoted respectively by z_0 and z_1, defined as $z_i = \frac{k_i^+}{q^+} = \frac{p_i^+}{q^+}$, and $\mathbf{x_i}$ denotes the transverse position of the (anti)quark. The four-momentum of the incoming photon is denoted by q^μ, k_i is the momentum of the incoming (anti)quark and p_i is the momentum of the outgoing (anti)quark. The color indices of the quark and antiquark before the interaction are denoted by α_i, while the color indices after interaction are denoted by β_i. The mixed space representation used here specifies the longitudinal momentum and transverse position of the quark and antiquark. This representation is useful in the case of interactions at a high-energy limit, since the longitudinal momentum is not modified in the scattering process, and neither are the transverse positions of

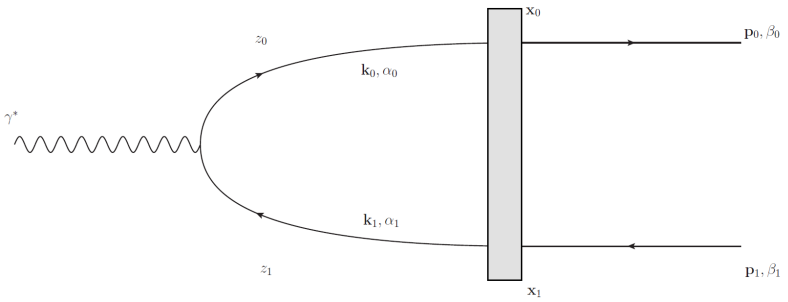

Figure 4. The leading order diagram of the splitting of a virtual photon into a dipole, which then interacts with the proton color field (gray area denotes the interaction). Since we consider inclusive jet production, the proton does not necessarily remain a proton after the interaction, since the final state can include any combination of hadrons.

the partons x_i. [19]

From a vacuum state $|0\rangle$, we obtain the $q\bar{q}$ state by acting on it with the quark and antiquark creation operators $b^\dagger$ and $d^\dagger$,

$$|q_{\alpha_0}\bar{q}_{\alpha_1}\rangle_{\text{mixed}} = b^\dagger(\mathbf{x_0}, z_0, \alpha_0, h_0)d^\dagger(\mathbf{x_1}, z_1, \alpha_1, h_1)\,|0\rangle\,, \tag{25}$$

where $h_i = \pm 1/2$ denotes helicity. When the quark state $|q_\alpha\rangle$ scatters off a target color field, it gains a phase, as discussed in Sec. 2.3, which is represented by a Wilson line, resulting in the state $U_{F\alpha\beta}\,|q_\beta\rangle$. For the antiquark state $|\bar{q}_\alpha\rangle$, we use the Hermitian conjugate of the Wilson line to obtain, after scattering, $U^\dagger_{F\beta\alpha}\,|\bar{q}_\beta\rangle$.

We obtain for the outgoing state after the scattering, still in mixed space representation,

$$\begin{aligned}\hat{S}\,|\gamma^*\rangle &= \sum_{q\bar{q}\text{ states}} \delta_{\alpha_0\alpha_1}\left[U_F(\mathbf{x_0})_{\alpha_0\beta_0}U_F^\dagger(\mathbf{x_1})_{\beta_1\alpha_1}\right]\Psi_{q\bar{q}}(z_0, z_1, \mathbf{x_0}, \mathbf{x_1})\,|q_{\beta_0}\bar{q}_{\beta_1}\rangle_{\text{mixed}} \\ &= \sum_{q\bar{q}\text{ states}} \left[U_F(\mathbf{x_0})U_F^\dagger(\mathbf{x_1})\right]_{\beta_0\beta_1}\Psi_{q\bar{q}}(z_0, z_1, \mathbf{x_0}, \mathbf{x_1})\,|q_{\beta_0}\bar{q}_{\beta_1}\rangle_{\text{mixed}}\,,\end{aligned} \tag{26}$$

where $\hat{S}$ is the S-operator which depends on the classical gluon field. [5] In the massless quark case, the function $\Psi_{q\bar{q}}(z_0, z_1, \mathbf{x_0}, \mathbf{x_1})$ is written explicitly as [4]

$$\begin{aligned}\Psi_{q\bar{q}}(z_0, z_1, \mathbf{x_0}, \mathbf{x_1}, h_0, h_1) =& (2\pi)^2 2ee_f\sqrt{z_0z_1}\delta(z_0 + z_1 - 1) \\ &\times \Phi^{\text{LO}}_{\text{T,L}}(z_0, z_1, \mathbf{x_0}, \mathbf{x_1}, (h_0), \lambda)\delta_{h_0,-h_1}\,,\end{aligned} \tag{27}$$

where ee_f is the electric charge of the quark f, and the longitudinal (L) and trans-

verse (T) functions Φ are written as

$$\Phi_{\mathrm{L}}^{\mathrm{LO}}(z_0, z_1, \mathbf{x_0}, \mathbf{x_1}) = -2z_0 z_1 Q K_0\left(Q\sqrt{z_0 z_1 x_{01}^2}\right), \tag{28}$$

$$\begin{aligned}\Phi_{\mathrm{T}}^{\mathrm{LO}}(z_0, z_1, \mathbf{x_0}, \mathbf{x_1}, h_0, \lambda) =& i[z_1 - z_0 - 2h_0\lambda]\frac{\epsilon_\lambda \cdot \mathbf{x}_{01}}{x_{01}^2} Q\sqrt{z_0 z_1 x_{01}^2} \\ & \times K_1\left(Q\sqrt{z_0 z_1 x_{01}^2}\right).\end{aligned} \tag{29}$$

Here, the notations $\mathbf{x}_{ij} = \mathbf{x}_i - \mathbf{x}_j$ and $x_{ij} = |\mathbf{x}_{ij}|$ have been used, $\lambda = \pm 1$ signifies the helicity of the transverse photon, and K_0 and K_1 are modified Bessel functions of the second kind. Here, ϵ_λ is the transverse polarization vector for transverse gauge bosons of helicity λ which satisfies the relation [19]

$$\sum_{\lambda=\pm 1} \epsilon_\lambda^{i*}\epsilon_\lambda^{j} = \delta^{ij}. \tag{30}$$

The mixed space states can alternatively be written in momentum space representation with the use of a Fourier transform. For the outgoing state, this reads

$$\begin{aligned}\hat{S}\left|\gamma^*\right\rangle = \sum_{q\bar{q}\text{ states}} \int \frac{\mathrm{d}^2\mathbf{x_0}}{2\pi} \int \frac{\mathrm{d}^2\mathbf{x_1}}{2\pi} e^{-i\mathbf{p_0}\cdot\mathbf{x_0}} e^{-i\mathbf{p_1}\cdot\mathbf{x_1}} \left[U_F(\mathbf{x_0})U_F^\dagger(\mathbf{x_1})\right]_{\beta_0\beta_1} \\ \times \Psi_{q\bar{q}}(z_0, z_1, \mathbf{x_0}, \mathbf{x_1}) \left|q_{\beta_0}\bar{q}_{\beta_1}\right\rangle_{\mathrm{mom}}.\end{aligned} \tag{31}$$

Here, $\mathbf{p_i}$ signifies the transverse momentum of the quarks after interaction. The S-matrix of the process is, in the CGC effective theory, given by the overlap of the incoming and outgoing states. [4] The S-matrix for this process is

$$S_{q\bar{q}\leftarrow\gamma} = \left\langle \bar{q}_{\beta_1}(\mathbf{p_1}, z_1, h_1) q_{\beta_0}(\mathbf{p_0}, z_0, h_0) | \hat{S} | \gamma^* \right\rangle. \tag{32}$$

Plugging in the mixed space representations of the incoming and outgoing states, we obtain an explicit form for the S-matrix of the process:

$$S_{q\bar{q}\leftarrow\gamma} = \int \frac{\mathrm{d}^2\mathbf{x_0}}{2\pi} \int \frac{\mathrm{d}^2\mathbf{x_1}}{2\pi} e^{-i\mathbf{p_0}\cdot\mathbf{x_0}} e^{-i\mathbf{p_1}\cdot\mathbf{x_1}} \left[U_F(\mathbf{x_0})U_F^\dagger(\mathbf{x_1})\right]_{\beta_0\beta_1} \Psi_{q\bar{q}}(z_0, z_1, \mathbf{x_0}, \mathbf{x_1}). \tag{33}$$

From the explicit form (33) of the S-matrix, the forward scattering amplitude

$M_{q\bar{q}\leftarrow\gamma}$ for the process can be shown to be [4]

$$2\pi(2q^+)\delta(k_0^+ + k_1^+ - q^+)M_{q\bar{q}\leftarrow\gamma} = \int \frac{\mathrm{d}^2\mathbf{x_0}}{2\pi}\int \frac{\mathrm{d}^2\mathbf{x_1}}{2\pi} e^{-i\mathbf{p_0}\cdot\mathbf{x_0}} e^{-i\mathbf{p_1}\cdot\mathbf{x_1}} \times \left(\Big[U_F(\mathbf{x_0})U_F^\dagger(\mathbf{x_1})\Big]_{\beta_0\beta_1} - \delta_{\beta_0\beta_1}\right)\Psi_{q\bar{q}}(z_0, z_1, \mathbf{x_0}, \mathbf{x_1}). \tag{34}$$

Using Eq. (34) for the forward scattering amplitude , we get the following form for the dijet cross section:

$$(2\pi)^6 2p_0^+ 2p_1^+ \frac{\mathrm{d}\sigma^{\mathrm{dijet}}}{\mathrm{d}p_0^+\mathrm{d}p_1^+\mathrm{d}^2\mathbf{p_0}d^2\mathbf{p_1}} = \sum_{\beta_i h_i f} 2\pi(2q^+)\delta(k_0^+ + k_1^+ - q^+)\langle|M_{q\bar{q}\leftarrow\gamma}|^2\rangle_C. \tag{35}$$

Here, $\langle ...\rangle_C$ stands for averaging over the target color configurations. This has to be done, as the specific color configuration of the target is unknown.

To obtain an expression for the square of forward scattering amplitude, we first insert Eq. (27) into Eq. (34) to get

$$M_{q\bar{q}\leftarrow\gamma} = (2\pi)ee_f\sqrt{z_0 z_1}\int \frac{\mathrm{d}^2\mathbf{x_0}}{2\pi}\int \frac{\mathrm{d}^2\mathbf{x_1}}{2\pi} e^{-i\mathbf{p_0}\cdot\mathbf{x_0}} e^{-i\mathbf{p_1}\cdot\mathbf{x_1}} \times \left(\Big[U_F(\mathbf{x_0})U_F^\dagger(\mathbf{x_1})\Big]_{\beta_0\beta_1} - \delta_{\beta_0\beta_1}\right)\Phi_{\mathrm{T,L}}^{\mathrm{LO}}(\mathbf{x_0}, \mathbf{x_1}, z_0, z_1, (h_0), \lambda)\delta_{h_0,-h_1}. \tag{36}$$

Then, multiplying Eq. (36) with its complex conjugate we get for the amplitude squared:

$$\begin{aligned}|M_{q\bar{q}\leftarrow\gamma}|^2 = (2\pi)^2(ee_f)^2 z_0 z_1 &\int \frac{\mathrm{d}^2\mathbf{x_0}}{2\pi}\int \frac{\mathrm{d}^2\mathbf{x_1}}{2\pi} e^{-i\mathbf{p_0}\cdot\mathbf{x_0}} e^{-i\mathbf{p_1}\cdot\mathbf{x_1}} \\ &\times \left(\Big[U_F(\mathbf{x_0})U_F^\dagger(\mathbf{x_1})\Big]_{\beta_0\beta_1} - \delta_{\beta_0\beta_1}\right)\Phi_{\mathrm{T,L}}^{\mathrm{LO}}(\mathbf{x_0}, \mathbf{x_1}, z_0, z_1, (h_0), \lambda)\delta_{h_0,-h_1} \\ &\times \int \frac{\mathrm{d}^2\mathbf{x_0'}}{2\pi}\int \frac{\mathrm{d}^2\mathbf{x_1'}}{2\pi} e^{+i\mathbf{p_0}\cdot\mathbf{x_0'}} e^{+i\mathbf{p_1}\cdot\mathbf{x_1'}} \\ &\times \left(\Big[U_F(\mathbf{x_0'})U_F^\dagger(\mathbf{x_1'})\Big]_{\beta_0\beta_1} - \delta_{\beta_0\beta_1}\right)^* \Phi_{\mathrm{T,L}}^{\mathrm{LO}}(\mathbf{x_0'}, \mathbf{x_1'}, z_0, z_1, (h_0), \lambda)^*\delta_{h_0,-h_1}.\end{aligned} \tag{37}$$

Plugging Eq. (37) into Eq. (35), but ignoring the averaging over the target color configuration for now, we can see that the inclusive cross section equation before

color averaging becomes

$$\begin{aligned}\sum_{\beta_i h_i f}(2q^+)2\pi\delta(k_0^+ + k_1^+ - q^+)|M_{q\bar{q}\leftarrow\gamma}|^2 &= \left(\sum_f e_f^2\right) 4(2\pi)^4 z_0 z_1 \delta(z_0+z_1-1)\\ &\times \alpha_{\rm em}\int\frac{\mathrm{d}^2\mathbf{x_0}}{2\pi}\int\frac{\mathrm{d}^2\mathbf{x_1}}{2\pi}e^{-i\mathbf{p_0}\cdot\mathbf{x_0}}e^{-i\mathbf{p_1}\cdot\mathbf{x_1}}\int\frac{\mathrm{d}^2\mathbf{x_0'}}{2\pi}\int\frac{\mathrm{d}^2\mathbf{x_1'}}{2\pi}e^{+i\mathbf{p_0}\cdot\mathbf{x_0'}}e^{+i\mathbf{p_1}\cdot\mathbf{x_1'}}\\ &\times\sum_{\beta_i}\left(\left[U_F(\mathbf{x_0})U_F^\dagger(\mathbf{x_1})\right]_{\beta_0\beta_1}-\delta_{\beta_0\beta_1}\right)\left(\left[U_F(\mathbf{x_0'})U_F^\dagger(\mathbf{x_1'})\right]_{\beta_0\beta_1}-\delta_{\beta_0\beta_1}\right)^*\\ &\times\sum_{h_i}\delta_{h_0,-h_1}\Phi^{\rm LO}_{\rm T,L}(\mathbf{x_0},\mathbf{x_1},z_0,z_1,(h_0),\lambda)\Phi^{\rm LO}_{\rm T,L}(\mathbf{x_0'},\mathbf{x_1'},z_0,z_1,(h_0),\lambda)^*,\end{aligned} \tag{38}$$

where the fine structure constant $\alpha_{\rm em} = e^2/(4\pi)$, where e is the elementary charge. We can calculate the Φ-terms separately for transverse and longitudinal polarization contributions. For a longitudinally polarized photon, from Eq. (28) we straightforwardly obtain

$$\begin{aligned}&\sum_{h_0,h_1}\delta_{h_0,-h_1}\Phi^{\rm LO}_{\rm L}(\mathbf{x_0},\mathbf{x_1},z_0,z_1)\Phi^{\rm LO}_{\rm L}(\mathbf{x_0'},\mathbf{x_1'},z_0,z_1)^*\\ &\qquad = 8z_0^2z_1^2Q^2K_0\left(Q\sqrt{z_0z_1x_{01}^2}\right)K_0\left(Q\sqrt{z_0z_1x_{1'0'}^2}\right).\end{aligned} \tag{39}$$

For a transversely polarized photon, we use Eq. (29) to obtain

$$\begin{aligned}&\sum_{h_0,h_1}\delta_{h_0,-h_1}\Phi^{\rm LO}_{\rm T}(\mathbf{x_0},\mathbf{x_1},z_0,z_1,h_0,\lambda)\Phi^{\rm LO}_{\rm T}(\mathbf{x_0'},\mathbf{x_1'},z_0,z_1,h_0,\lambda)^*\\ &\quad = 4[z_0^2+z_1^2]\left(\frac{\epsilon_\lambda\cdot\mathbf{x}_{01}}{x_{01}^2}\right)\left(\frac{\epsilon_\lambda^*\cdot\mathbf{x}_{1'0'}}{x_{1'0'}^2}\right)\\ &\quad\times\left[Q\sqrt{z_0z_1x_{01}^2}K_1\left(Q\sqrt{z_0z_1x_{01}^2}\right)\right]\left[Q\sqrt{z_0z_1x_{1'0'}^2}K_1\left(Q\sqrt{z_0z_1x_{1'0'}^2}\right)\right].\end{aligned} \tag{40}$$

We can now average Eq. (40) over λ to remove the λ-dependency, with the help of the property (30) of polarization vectors:

$$\begin{aligned}&\frac{1}{2}\sum_{\lambda=\pm1}(\epsilon_\lambda\epsilon_\lambda^*)\,4[z_0^2+z_1^2]\,\frac{\mathbf{x}_{01}\cdot\mathbf{x}_{1'0'}}{x_{01}^2x_{1'0'}^2}\left[Q\sqrt{z_0z_1x_{01}^2}K_1\left(Q\sqrt{z_0z_1x_{01}^2}\right)\right]\\ &\qquad\times\left[Q\sqrt{z_0z_1x_{1'0'}^2}K_1\left(Q\sqrt{z_0z_1x_{1'0'}^2}\right)\right]\\ &\quad = 2[z_0^2+z_1^2]\frac{\mathbf{x}_{01}\cdot\mathbf{x}_{1'0'}}{x_{01}^2x_{1'0'}^2}\left[Q\sqrt{z_0z_1x_{01}^2}K_1\left(Q\sqrt{z_0z_1x_{01}^2}\right)\right]\\ &\qquad\times\left[Q\sqrt{z_0z_1x_{1'0'}^2}K_1\left(Q\sqrt{z_0z_1x_{1'0'}^2}\right)\right].\end{aligned} \tag{41}$$

Next, we assess the terms which include Wilson lines. The sum over β_0 and β_1 of the Wilson line factors is written as

$$\begin{aligned}
&\sum_{\beta_i}\Big(\Big[U_F(\mathbf{x_0})U_F^\dagger(\mathbf{x_1})\Big]_{\beta_0\beta_1}-\delta_{\beta_0\beta_1}\Big)\Big(\Big[U_F(\mathbf{x_0'})U_F^\dagger(\mathbf{x_1'})\Big]_{\beta_0\beta_1}-\delta_{\beta_0\beta_1}\Big)^*\\
&=\sum_{\beta_i}\Big(\Big[U_F(\mathbf{x_0})U_F^\dagger(\mathbf{x_1})\Big]_{\beta_0\beta_1}\Big[U_F(\mathbf{x_1'})U_F^\dagger(\mathbf{x_0'})\Big]_{\beta_1\beta_0}-\delta_{\beta_0\beta_1}\Big[U_F(\mathbf{x_0})U_F^\dagger(\mathbf{x_1})\Big]_{\beta_0\beta_1}\\
&\qquad\qquad-\delta_{\beta_0\beta_1}\Big[U_F(\mathbf{x_1'})U_F^\dagger(\mathbf{x_0'})\Big]_{\beta_1\beta_0}+\delta_{\beta_0\beta_1}\Big)\\
&=N_c\Big(\frac{1}{N_c}\mathrm{Tr}\Big(U_F(\mathbf{x_0})U_F^\dagger(\mathbf{x_1})U_F(\mathbf{x_1'})U_F^\dagger(\mathbf{x_0'})\Big)-\frac{1}{N_c}\mathrm{Tr}\Big(U_F(\mathbf{x_0})U_F^\dagger(\mathbf{x_1})\Big)\\
&\qquad\qquad-\frac{1}{N_c}\mathrm{Tr}\Big(U_F(\mathbf{x_1'})U_F^\dagger(\mathbf{x_0'})\Big)+1.\Big)
\end{aligned}\tag{42}$$

Noticing that the only color-dependence in Eq. (38) comes from the Wilson line terms, the color configuration averaging $\langle ...\rangle_C$ has to be done only for the terms in Eq. (42). We use the notation S_{01} to denote the usual dipole operator in the fundamental representation,

$$S_{01}=\left\langle\frac{1}{N_c}\mathrm{Tr}\Big(U_F(\mathbf{x_0})U_F^\dagger(\mathbf{x_1})\Big)\right\rangle_C.\tag{43}$$

We can also write this in terms of the dipole amplitude $\mathcal{N}_{01}$, as $S_{01}=1-\mathcal{N}_{01}$. Thus, we have for the inclusive dijet cross section

$$\begin{aligned}
(2\pi)^6p_0^+p_1^+\frac{\mathrm{d}\sigma^{\mathrm{dijet}}}{\mathrm{d}p_0^+\mathrm{d}p_1^+\mathrm{d}^2\mathbf{p_0}\mathrm{d}^2\mathbf{p_1}}&=\alpha_{\mathrm{em}}(2\pi)^4\left(\sum_f e_f^2\right)z_0z_1\delta(z_0+z_1-1)\\
&\times\int\frac{\mathrm{d}^2\mathbf{x_0}}{2\pi}\int\frac{\mathrm{d}^2\mathbf{x_1}}{2\pi}e^{-i\mathbf{p_0}\cdot\mathbf{x_0}}e^{-i\mathbf{p_1}\cdot\mathbf{x_1}}\int\frac{\mathrm{d}^2\mathbf{x_0'}}{2\pi}\int\frac{\mathrm{d}^2\mathbf{x_1'}}{2\pi}e^{+i\mathbf{p_0}\cdot\mathbf{x_0'}}e^{+i\mathbf{p_1}\cdot\mathbf{x_1'}}\\
&\times N_c\left(\left\langle\frac{1}{N_c}\mathrm{Tr}\Big(U_F(\mathbf{x_0})U_F^\dagger(\mathbf{x_1})U_F(\mathbf{x_1'})U_F^\dagger(\mathbf{x_0})\Big)\right\rangle_C-S_{01}-S_{01'}+1\right)\\
&\times\sum_{h_i}\delta_{h_0,-h_1}\Phi^{\mathrm{LO}}_{\mathrm{T,L}}(\mathbf{x_0},\mathbf{x_1},z_0,z_1,(h_0),\lambda)\Phi^{\mathrm{LO}}_{\mathrm{T,L}}(\mathbf{x_0'},\mathbf{x_1'},z_0,z_1,(h_0),\lambda)^*,
\end{aligned}\tag{44}$$

with the $\Phi^{\mathrm{LO}}_{\mathrm{T,L}}$-terms as in Eqs. (39) and (41). A very similar expression was also reached in Ref. [4], just with a slight difference in the third line containing the Wilson line terms, arising from the fact that the calculation in Ref. [4] is done for exclusive processes while our process is inclusive. Thus, we have managed to effectively reproduce the equation in Ref. [4] for the dijet cross section.

To get a step closer to the inclusive one-jet cross section, we integrate Eq. (44)

over the transverse momentum of the other jet, $d^2\mathbf{p_0}$. This gives us a function proportional to $\delta^{(2)}(\mathbf{x_0}-\mathbf{x_0'})$, and therefore the cross section becomes of the form

$$\begin{aligned}(2\pi)^6 p_0^+ p_1^+ \frac{\mathrm{d}\sigma}{\mathrm{d}p_0^+\mathrm{d}p_1^+\mathrm{d}^2\mathbf{p_1}} &= \alpha_{\mathrm{em}}(2\pi)^5 \left(\sum_f e_f^2\right) z_0 z_1 \delta(z_0+z_1-1) \\ &\times \int \frac{\mathrm{d}^2\mathbf{x_0}}{2\pi}\int \frac{\mathrm{d}^2\mathbf{x_1}}{2\pi}\int \frac{\mathrm{d}^2\mathbf{x_1'}}{2\pi} e^{-i\mathbf{p_1}\cdot(\mathbf{x_1}-\mathbf{x_1'})} \\ &\times N_c\left(\left\langle \frac{1}{N_c}\mathrm{Tr}\left(U_F(\mathbf{x_0})U_F^\dagger(\mathbf{x_1})U_F(\mathbf{x_1'})U_F^\dagger(\mathbf{x_0})\right)\right\rangle_C - S_{01} - S_{01'} + 1\right) \\ &\times \sum_{h_i}\delta_{h_0,-h_1}\Phi^{\mathrm{LO}}_{\mathrm{T,L}}(\mathbf{x_0},\mathbf{x_1},z_0,z_1,(h_0),\lambda)\Phi^{\mathrm{LO}}_{\mathrm{T,L}}(\mathbf{x_0},\mathbf{x_1'},z_0,z_1,(h_0),\lambda)^*.\end{aligned} \tag{45}$$

We notice that now our trace of four Wilson lines actually reduces to a two-line trace due to the cyclic property of traces and the unitarity of the Wilson lines:

$$\left\langle \frac{1}{N_c}\mathrm{Tr}\left(U_F(\mathbf{x_0})U_F^\dagger(\mathbf{x_1})U_F(\mathbf{x_1'})U_F^\dagger(\mathbf{x_0})\right)\right\rangle_C = \left\langle \frac{1}{N_c}\mathrm{Tr}\left(U_F^\dagger(\mathbf{x_1})U_F(\mathbf{x_1'})\right)\right\rangle_C = S_{11'}. \tag{46}$$

Thus, the terms on the third line of Eq. (45) can be written as

$$S_{11'} - S_{01} - S_{01'} + 1 = (1-S_{01}) + (1-S_{01'}) - (1-S_{11'}) = \mathcal{N}_{01} + \mathcal{N}_{01'} - \mathcal{N}_{11'}. \tag{47}$$

We change our variables to simplify notation, defining the new variables $\epsilon^2 = z_0 z_1 Q^2$, $\mathbf{r} = \mathbf{x_{01}} = (\mathbf{x_0}-\mathbf{x_1})$, $\mathbf{r'} = \mathbf{x_{0'1'}} = (\mathbf{x_0'}-\mathbf{x_1'})$, $\mathbf{b} = (\mathbf{x_0}+\mathbf{x_1})/2$ and $\mathbf{b'} = (\mathbf{x_0'}+\mathbf{x_1'})/2$. Here, $\mathbf{r}$ and $\mathbf{b}$ are the $q\bar{q}$ dipole transverse separation vector and the dipole impact parameter, respectively, with $\mathbf{r'}$ and $\mathbf{b'}$ as their counterparts in the complex conjugate of the amplitude. These changes to the variables result in a cross section of the form

$$\begin{aligned}p_0^+ p_1^+ \frac{\mathrm{d}\sigma_L}{\mathrm{d}p_0^+\mathrm{d}p_1^+\mathrm{d}^2\mathbf{p_1}} &= \alpha_{\mathrm{em}}\frac{N_c}{(2\pi)^4}\left(\sum_f e_f^2\right) z_0 z_1 \delta(z_0+z_1-1) \\ &\times \int \mathrm{d}^2\mathbf{r}\int \mathrm{d}^2\mathbf{r'} e^{+i\mathbf{p_1}\cdot(\mathbf{r}-\mathbf{r'})}\int \mathrm{d}^2\mathbf{b}\left(\mathcal{N}_{01}(\mathbf{r},\mathbf{b}) + \mathcal{N}_{01'}(\mathbf{r'},\mathbf{b}) - \mathcal{N}_{11'}(\mathbf{r}-\mathbf{r'},\mathbf{b})\right) \\ &\times 8 z_0 z_1 \epsilon^2 K_0\left(\epsilon|\mathbf{r}|\right) K_0\left(\epsilon|\mathbf{r'}|\right),\end{aligned} \tag{48}$$

for longitudinally polarized photons, and of the form

$$\begin{aligned} p_0^+ p_1^+ \frac{\mathrm{d}\sigma_T}{\mathrm{d}p_0^+ \mathrm{d}p_1^+ \mathrm{d}^2\mathbf{p_1}} &= \alpha_{\mathrm{em}} \frac{N_c}{(2\pi)^4} \left(\sum_f e_f^2 \right) z_0 z_1 \delta(z_0 + z_1 - 1) \\ &\times \int \mathrm{d}^2\mathbf{r} \int \mathrm{d}^2\mathbf{r}' e^{+i\mathbf{p_1}\cdot(\mathbf{r}-\mathbf{r}')} \int \mathrm{d}^2\mathbf{b} \left(\mathcal{N}_{01}(\mathbf{r},\mathbf{b}) + \mathcal{N}_{01'}(\mathbf{r}',\mathbf{b}) - \mathcal{N}_{11'}(\mathbf{r}-\mathbf{r}',\mathbf{b}) \right) \\ &\times 2[z_0^2 + z_1^2] \, \frac{\mathbf{r}\cdot\mathbf{r}'}{r^2 r'^2} \epsilon|\mathbf{r}| K_1\left(\epsilon|\mathbf{r}|\right) \epsilon|\mathbf{r}'| K_1\left(\epsilon|\mathbf{r}'|\right), \end{aligned} \tag{49}$$

for transversely polarized photons.

Once applying the variable changes $z_i = p_i^+/q^+$ and integrating over z_0, as well as denoting $r = |\mathbf{r}|$, we obtain expressions for the one-jet inclusive cross section for both longitudinally (L) and transversely (T) polarized photons:

$$\begin{aligned} \frac{\mathrm{d}\sigma_L}{\mathrm{d}^2\mathbf{p_1}} &= \frac{\alpha_{\mathrm{em}} N_c}{(2\pi)^4} \left(\sum_f e_f^2 \right) \int \mathrm{d}^2\mathbf{r} \mathrm{d}^2\mathbf{r}' dz_1 e^{+i\mathbf{p_1}\cdot(\mathbf{r}-\mathbf{r}')} \\ &\times 8(z_1(1-z_1))\epsilon^2 K_0\left(\epsilon r\right) K_0\left(\epsilon r'\right) \\ &\times \int \mathrm{d}^2\mathbf{b} \left(\mathcal{N}_{01}(\mathbf{r},\mathbf{b}) + \mathcal{N}_{01'}(\mathbf{r}',\mathbf{b}) - \mathcal{N}_{11'}(\mathbf{r}-\mathbf{r}',\mathbf{b}) \right), \end{aligned} \tag{50}$$

$$\begin{aligned} \frac{\mathrm{d}\sigma_T}{\mathrm{d}^2\mathbf{p_1}} &= \frac{\alpha_{\mathrm{em}} N_c}{(2\pi)^4} \left(\sum_f e_f^2 \right) \int \mathrm{d}^2\mathbf{r} \mathrm{d}^2\mathbf{r}' \mathrm{d}z_1 e^{+i\mathbf{p_1}\cdot(\mathbf{r}-\mathbf{r}')} \\ &\times 2\Big[z_1^2 + (1-z_1)^2\Big] \, \frac{\mathbf{r}\cdot\mathbf{r}'}{r^2 r'^2} \epsilon^2 r K_1\left(\epsilon r\right) r' K_1\left(\epsilon r'\right) \\ &\times \int \mathrm{d}^2\mathbf{b} \left(\mathcal{N}_{01}(\mathbf{r},\mathbf{b}) + \mathcal{N}_{01'}(\mathbf{r}',\mathbf{b}) - \mathcal{N}_{11'}(\mathbf{r}-\mathbf{r}',\mathbf{b}) \right). \end{aligned} \tag{51}$$

To make the calculations simpler, we will assume that the impact parameter dependence of the dipole amplitude factorizes and we can replace

$$\int \mathrm{d}^2\mathbf{b} \to \sigma_0/2, \tag{52}$$

where the term $\sigma_0/2$ is the transverse area of the proton. [34] This factorization for the dipole amplitude calculations neglects the geometric details of the proton, and while it is useful in the case of the photon-proton interactions, it will, however, not be applicable in photon-nucleus calculations, where the geometry of the nucleus must be considered more carefully.

Starting with Eq. (50) for the one-jet inclusive cross section for longitudinally polarized photons, we can solve parts of the equation analytically to ease numerical

calculations. We see that, in the longitudinal case, for the first two dipole amplitude terms the only angular dependence can be found in the exponential term. The angle θ_r ($\theta_{r'}$) is the angle between $\mathbf{p_1}$ and $\mathbf{r}$ ($\mathbf{r'}$). Thus, we only have to perform the angular integration over the exponential term as follows:

$$\int_0^{2\pi} \mathrm{d}\theta_r \mathrm{d}\theta_{r'}\, e^{ip_1 r\cos\theta_r - ip_1 r'\cos\theta_{r'}} = (2\pi)^2 J_0(p_1 r) J_0(p_1 r'), \tag{53}$$

where J_0 is the Bessel function of the first kind and $p_1 = |\mathbf{p_1}|$. However, we see that although the first two dipole amplitudes are not angularly dependent, the third one, $\mathcal{N}(\mathbf{r}-\mathbf{r'})$, is. This means that the previously described angular integration does not apply to this term, and therefore this amplitude term has to be integrated numerically over the angles along with the exponential term.

We could yet further simplify the equation by noticing that the r integral can be analytically calculated in the second term, as can the r' integral in the first term. This is because

$$\int r\mathrm{d}r\, K_0(\epsilon r)\, J_0(p_1 r) = \frac{1}{p_1^2+\epsilon^2}, \tag{54}$$

where the result of the integral is essentially the wave function of the longitudinal photon in momentum space. Performing the r integral analytically is tested in our numerical analysis, but the effect on our results is minimal at least in the kinematic region and with integration method used.

3.2 Inclusion of quark mass

We want to include the quark mass m_f (where f symbolizes a specific flavor) in our calculations. This is achieved in the case of the longitudinally polarized photon through the substitution [4]

$$\epsilon^2 \to \epsilon_f^2 = z_0 z_1 Q^2 + m_f^2. \tag{55}$$

This substitution can be directly plugged into Eq. (50) to include the quark mass in the longitudinal cross section. In the transverse polarization case, there is an additional term that appears in the cross section when accounting for the quark

mass. [4] The change is

$$\begin{aligned} & 2\left[z_1^2+(1-z_1)^2\right]\frac{\mathbf{r}\cdot\mathbf{r}'}{r^2r'^2}\epsilon^2 rK_1\left(\epsilon r\right)r'K_1\left(\epsilon r'\right) \\ \rightarrow\ & 2\Big[z_1^2+(1-z_1)^2\Big]\frac{\mathbf{r}\cdot\mathbf{r}'}{r^2r'^2}\epsilon_f^2 rK_1\left(\epsilon_f r\right)r'K_1\left(\epsilon_f r'\right)+m_f^2K_0\left(\epsilon_f r\right)K_0\left(\epsilon_f r'\right). \end{aligned} \tag{56}$$

With the replacement for the impact parameter integral (52), the angular integration (53) and inclusion of the quark mass (55), the longitudinal cross section for one-jet production (50) becomes

$$\begin{aligned} \frac{\mathrm{d}\sigma_L}{\mathrm{d}^2\mathbf{p_1}} =& \frac{\alpha_{\mathrm{em}}N_c}{(2\pi)^4}\left(\sum_f e_f^2\right)\sigma_0\int r\mathrm{d}r\,r'\mathrm{d}r'\,\mathrm{d}z_1 4(z_1(1-z_1))\epsilon_f^2K_0\left(\epsilon_f r\right)K_0\left(\epsilon_f r'\right) \\ & \times\Big[(2\pi)^2J_0(p_1r)J_0(p_1r')\left(\mathcal{N}(r)+\mathcal{N}(r')\right)) \\ & -\int_0^{2\pi}\mathrm{d}\theta_r\mathrm{d}\theta_{r'}\,e^{i\mathbf{p_1}\cdot(\mathbf{r}-\mathbf{r}')}\mathcal{N}(\mathbf{r}-\mathbf{r}')\Big], \end{aligned} \tag{57}$$

where ϵ_f^2 is now as shown in Eq. (55). The lower indices for the $\mathcal{N}$ terms have been dropped. We see that evaluating the term $\mathcal{N}(\mathbf{r}-\mathbf{r}')$ requires the angle between $\mathbf{r}$ and $\mathbf{r}'$, denoted by $\theta_{rr'}=\theta_r-\theta_{r'}$, and for the evaluation of the exponential term the angle between $\mathbf{p_1}$ and $\mathbf{r}-\mathbf{r}'$ is required. This means we keep the angular integration variables for the numerical calculation. Explicitly written, the equation used in the numerical integration is of the form

$$\begin{aligned} \frac{\mathrm{d}\sigma_L}{\mathrm{d}^2\mathbf{p_1}} =& \frac{\alpha_{\mathrm{em}}N_c}{(2\pi)^4}\left(\sum_f e_f^2\right)\sigma_0\int r\mathrm{d}r\,r'\mathrm{d}r'\,\mathrm{d}z_1 4(z_1(1-z_1))\epsilon_f^2K_0\left(\epsilon_f r\right)K_0\left(\epsilon_f r'\right) \\ & \times\Bigg[(2\pi)^2J_0(p_1r)J_0(p_1r')\left(\mathcal{N}(r)+\mathcal{N}(r')\right) \\ & -\int_0^{2\pi}\mathrm{d}\theta_r\mathrm{d}\theta_{r'}\,e^{ip_1r\cos(\theta_r)-ip_1r'\cos(\theta_{r'})}\mathcal{N}(\sqrt{r^2+r'^2-(2rr'\cos(\theta_{rr'}))})\Bigg]. \end{aligned} \tag{58}$$

Repeating the same process for the transverse cross section (51), we obtain a slightly different form of equation, as there are more terms dependent on the angles θ_r and $\theta_{r'}$. Using Eq. (52) for the impact parameter integral and Eq. (56) for inclusion of the mass term, we have the following form for the transverse cross

section:

$$\frac{\mathrm{d}\sigma_T}{\mathrm{d}^2\mathbf{p_1}} = \frac{\alpha_{\mathrm{em}}N_c}{(2\pi)^4}\left(\sum_f e_f^2\right)\sigma_0\int r\mathrm{d}r\, r'\mathrm{d}r'\int_0^{2\pi}\mathrm{d}\theta_r\mathrm{d}\theta_{r'}\,\mathrm{d}z_1 e^{ip_1 r\cos(\theta_r)-ip_1 r'\cos(\theta_{r'})}$$
$$\times\left\{\left[z_1^2+(1-z_1)^2\right]\,\cos(\theta_{rr'})\epsilon_f^2 K_1\left(\epsilon_f r\right)K_1\left(\epsilon_f r'\right)+m_f^2 K_0\left(\epsilon_f r\right)K_0\left(\epsilon_f r'\right)\right\} \quad (59)$$
$$\times\left(\mathcal{N}(r)+\mathcal{N}(r')-\mathcal{N}(\sqrt{r^2+r'^2-(2rr'\cos(\theta_{rr'}))})\right).$$

Eqs. (58) and (59) are the ones we use in our numerical analysis in Sec. 5.

3.3 From photon-proton to photon-nucleus interactions

Now that we have equations for jet production cross sections in photon-proton interactions, we want to obtain equations for photon-nucleus interactions. In the previous section, we used the replacement (52) to handle the **b** integral, since we assumed the impact parameter **b** to factorize in photon-proton interactions; this replacement thus took care of the impact parameter dependence of the dipole amplitude. However, in the case of photon-nucleus interactions we must take into account the geometry and **b**-dependent density of the nucleus, which requires handling the impact parameter as an integration parameter.

To compare the photon-proton and photon-nucleus cross sections, we define a nuclear suppression ratio R_{pA} such that

$$R_{pA} = \frac{\sigma_{\gamma A}}{A\sigma_{\gamma p}}. \quad (60)$$

This is a ratio between the photon-nucleus cross section $\sigma_{\gamma A}$ and the photon-proton cross section $\sigma_{\gamma p}$ scaled by the mass number A of the nucleus. The ratio is a good indicator of suppression effects in the nucleus, since in the case of no suppression, this ratio should be equal to one.

From the photon-proton dipole amplitude, denoted by $\mathcal{N}^p(r)$, we can follow Ref. [34] in using the optical Glauber model to obtain the dipole amplitude of a photon-nucleus interaction, $\mathcal{N}^A(\mathbf{r},\mathbf{b})$. The total quark-antiquark dipole-proton cross section reads

$$\sigma_{\mathrm{dip}}^p = \sigma_0\mathcal{N}^p(r), \quad (61)$$

where σ_0 is the same parameter that appears in Eq. (52) and r is the size of the dipole. The amplitude $\mathcal{N}^p(r)$ (22) is as discussed in Sec. 2.3.

At the limit of very small dipoles, the dipole-nucleus cross section should solely be a sum of dipole-proton cross sections, that is, $\sigma^A_{\rm dip} = A\sigma^p_{\rm dip}$. However, at the limit of large dipoles we should have $\mathrm{d}\sigma^A_{\rm dip}/\mathrm{d}^2\mathbf{b} \equiv 2\mathcal{N}^A(\mathbf{r},\mathbf{b}) \leq 2$. According to Ref. [34], to satisfy the equations at both limits, the dipole-nucleus scattering amplitude is written in an exponential form

$$\mathcal{N}^A(\mathbf{r},\mathbf{b}) = \left[1 - \exp\left(-\frac{AT_A(\mathbf{b})}{2}\sigma^p_{\rm dip}\right)\right], \tag{62}$$

where $T_A(\mathbf{b})$ is the Woods-Saxon nuclear density, or transverse thickness function of the nucleus, obtained by integrating the Woods-Saxon distribution

$$\rho_A(\mathbf{b},z) = \frac{n}{1+\exp\left[\frac{\sqrt{\mathbf{b}^2+z^2}-R_A}{d}\right]} \tag{63}$$

over the longitudinal distance z. In Eq. (63), the parameters used are $d = 0.54$ fm, $R_A = (1.12A^{1/3} - 0.86A^{-1/3})$ fm and n as given by the normalization to unity as $\int \mathrm{d}^2\mathbf{b}\,\mathrm{d}z\,\rho_A(\mathbf{b},z) = 1$.

If Eq. (62) is used directly to compute particle production, we run into a problem at large r as the S-matrix element $S = 1 - \mathcal{N}$ approaches a non-zero limit. This causes the dipole gluon distribution to develop unphysical oscillations, so the cross section in Eq. (62) has to be expanded. In the exponent of Eq. (62) we therefore use the expansion suggested in Ref. [34],

$$\sigma^p_{\rm dip} = \sigma_0\mathcal{N}^p(\mathbf{r}) \approx \sigma_0\frac{\mathbf{r}^2Q^2_{s0}}{4}\ln\left(\frac{1}{|\mathbf{r}|\Lambda_{\rm QCD}} + e_c\cdot e\right). \tag{64}$$

Here, as in Eq. (22), Q^2_{s0} is the initial saturation scale and the constant $e_c \cdot e$ works as an infrared cutoff, e being Euler's number.

Now, plugging into Eq. (62) the approximation (64), we have

$$\mathcal{N}^A(\mathbf{r},\mathbf{b}) = 1 - \exp\left[-AT_A(\mathbf{b})\frac{\sigma_0}{2}\frac{\mathbf{r}^2Q^2_{s0}}{4}\ln\left(\frac{1}{|\mathbf{r}|\Lambda_{\rm QCD}} + e_c\cdot e\right)\right]. \tag{65}$$

The dipole-nucleus amplitudes can be obtained by solving the rcBK evolution equation (see Sec. 2.3) by using Eq. (65) as a non-perturbative input at an initial $x = x_0 = 0.01$. The scattering amplitudes for each $\mathbf{b}$ have to be calculated separately, since a fully impact parameter dependent BK equation is not yet feasible to solve. The scattering amplitudes for each $\mathbf{b}$ have been calculated [34, 36], and in

this work these tabulated results are used.

Next, we can calculate the invariant yield $\mathrm{d}N(\mathbf{b})/\mathrm{d}^2p_T$ for each impact parameter $\mathbf{b}$ in the same manner as the cross sections were calculated for the proton-photon interactions, except now the dipole amplitudes $\mathcal{N}$ are different and depend on $\mathbf{b}$, and there is no σ_0 term. Then, from this result we can obtain the photon-nucleus cross section by integrating over it by $\mathbf{b}$,

$$\frac{\mathrm{d}\sigma_A}{\mathrm{d}^2p_T} = \int \mathrm{d}^2\mathbf{b}\, \frac{\mathrm{d}N(\mathbf{b})}{\mathrm{d}^2p_T} = 2\pi \int \mathrm{d}\mathbf{b}\, \mathbf{b} \frac{\mathrm{d}N(\mathbf{b})}{\mathrm{d}^2p_T}. \tag{66}$$

The saturation scale Q_s^2 of the nucleus can be calculated as the solution of $\mathcal{N}(\mathbf{r}^2 = 2/Q_s^2, \mathbf{b}) = 1 - e^{-1/2}$. A comparison of the saturation scales of a gold nucleus and proton at $x = 10^{-2}$ and $x = 10^{-4}$ are shown in Fig. 5. The figure depicts how the saturation scale of the nucleus intersects the proton saturation scale at around $|\mathbf{b}| = b \approx 30\ \mathrm{GeV}^{-1}$ and falls below it at larger b. At the large b scale, the nucleus is on average less dense than the proton. However, at large b, the scattering amplitude increases rapidly, and therefore at large energies the nucleus effectively grows rapidly on the edges. This signifies a large, unphysical increase in gluon density in the large b scale. Taking the physics of confinement into account in the BK equation would limit this behavior, but this is not feasible. For the large b scale, the dipole amplitude parametrization (65) is therefore not reliable, so we choose another way to handle calculations in this scale. This is done simply by choosing to scale the cross sections from the proton-photon interactions, assuming the nuclear suppression factor $R_{pA} = 1$ for large impact parameters, as suggested in Ref. [34].

We then see that, at small r, the dipole-proton (22) and dipole-nucleus (65) scattering amplitudes differ only by a factor:

$$\mathcal{N}^A(\mathbf{r}, \mathbf{b}) = AT_A(\mathbf{b}) \frac{\sigma_0}{2} \mathcal{N}^p(\mathbf{r}). \tag{67}$$

This means that we can now calculate the cross sections also in the region of large impact parameters, which are chosen to be above $b_0 = 30\,\mathrm{GeV}^{-1}$. The final equation for the photon-nucleus jet production cross section reads

$$\frac{\mathrm{d}\sigma_A}{\mathrm{d}^2p_T} = 2\pi \int_0^{b_0} \mathrm{d}\mathbf{b}\, \mathbf{b} \frac{\mathrm{d}N(\mathbf{b})}{\mathrm{d}^2p_T} + 2\pi \int_{b_0}^{\infty} \mathrm{d}\mathbf{b}\, \mathbf{b} AT_A(\mathbf{b}) \frac{\sigma_0}{2} \mathcal{N}^p(\mathbf{r}). \tag{68}$$

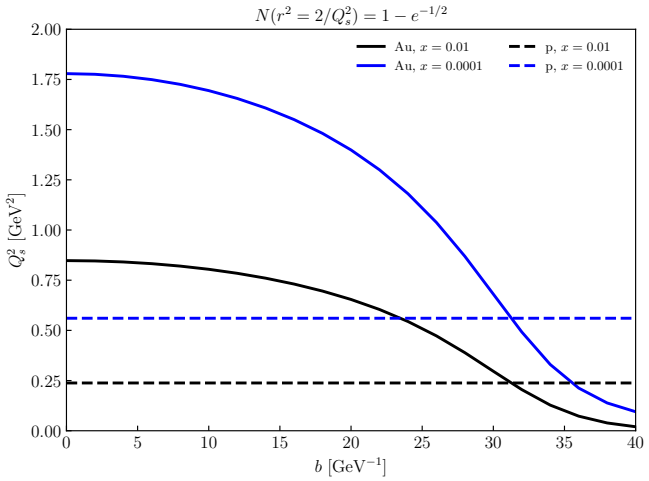

Figure 5. The saturation scale of a gold nucleus (Au, solid lines) and a proton (p, dashed lines) at $x = 10^{-2}$ and $x = 10^{-4}$ as a function of impact parameter $b = |\mathbf{b}|$, calculated using the MV^e parametrization model for the dipole amplitude.

4 Future experiments

Previous experiments which have provided data for the study of DIS processes and saturation effects include HERA at DESY, the LHC at CERN and RHIC at BNL. While at HERA, electrons were collided with protons and this allowed for the direct study of DIS, the LHC and RHIC collide beams of protons and heavy nuclei, and offer an insight into DIS-like processes through ultraperipheral collisions. The Electron-Ion Collider (EIC), the world's first electron-nucleus collider, will be a new experimental facility in the US, designed to be built at BNL within the next decade. [2] The focus of the EIC will be on gluon saturation physics, made possible by colliding electrons with heavy nuclei. This will enable the probing of gluon densities much higher than those seen in previous experiments.

The EIC is designed to collide highly polarized (70%) high-energy electron beams with high-energy ion beams ranging from polarized protons to very heavy nuclei. The layout of the facility is shown in Fig. 6. As compared to the only previously existing e-p collider, HERA, the EIC with its wide variety of polarized and heavy-ion beams as well as a significantly larger luminosity (by two to three orders of magnitude) and energy variablility offers wider capabilities to study gluon distributions and saturation effects. With the use of these properties, the EIC is expected to shine light on how sea quarks and gluons, including their spins, are distributed inside nucleons, as well as assess the boundary between saturation and dilute regimes. Whereas the e-p collisions at HERA achieved a center-of-mass energy $\sqrt{s}$ of about 318 GeV, the EIC is planned to function at energy ranges of $\sqrt{s} = 30 - 145$ GeV for e-p collisions and $\sqrt{s} = 20 - 90$ GeV for e-A collisions. [2] Knowing that $x \sim Q^2/s$, we can compute for a set value of Q^2, say, $5\,\mathrm{GeV}^2$, that these energies result in the corresponding ranges $x_p \approx 10^{-5}$ for HERA and $10^{-4} \lesssim x_p \lesssim 10^{-1}$ for EIC e-p and e-A collisions.

Other experimental setups to probe gluon saturation physics have been planned as well. At CERN, a Large Hadron-electron Collider (LHeC) has been designed as an extension of the present LHC in order to study DIS at higher energies. [3] In addition to electron-proton collisions, the LHeC would enable the colliding of lead ions with electrons, making it possible to study nuclear DIS at CERN. This planned TeV

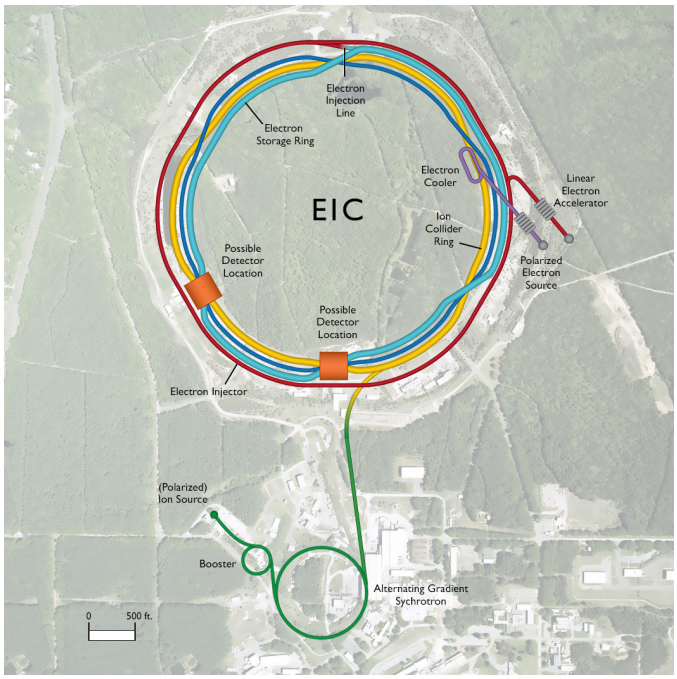

Figure 6. The layout of the EIC experiment at BNL. One ion accelerator/storage ring circulates the ions ranging from protons to heavy nuclei (yellow ring), and separate accelerator (red) and storage (light blue) rings hold the high-energy electrons. Figure from [37].

energy scale electron-hadron collider would be able to make measurements at much lower values of Bjorken x than possible in HERA, extending to $x = 10^{-6}$. It would also operate at a higher luminosity and produce heavier mass particles for study, such as the Higgs particle or top quarks. The beams would not be polarized, unlike in the EIC. In the more distant future, the LHeC has been envisioned to work together with the High-Luminosity Large Hadron Collider (HL-LHC) [3], an upgrade of the LHC planned for the end of this decade. Also, a long-term future plan involving a High-Energy LHC (HE-LHC) and a future circular hadron-hadron, electron-hadron and electron-positron collider (FCC) complex has been announced. [38]

The center-of-mass energy anticipated at the LHeC is 1.3 TeV before the LHC update, 1.77 TeV with the HE-LHC and 2.2 or 3.46 TeV with the FCC. At $Q^2 = 5\,\mathrm{GeV}^2$, these energies correspond to minimum momentum fractions x_p of size scale 10^{-6} for the LHeC alone and with the HL-LHC, and even of the scale 10^{-7} with the FCC. Predicted coverage of the kinematic plane in lepton-proton scattering of these experiments and others is presented in Fig. 7, which illustrates well just how small values of x can be reached by the LHeC and FCC as compared to the other experiments.

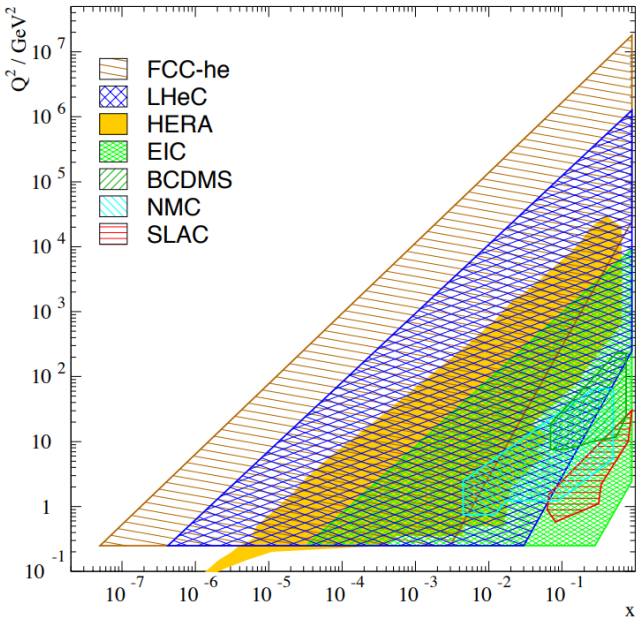

Figure 7. The kinematic plane coverage in lepton-proton DIS of different fixed target experiments (SLAC with electrons, NMS and BCDMS with muons) and electron-proton colliders EIC, HERA, LHeC and FCC-he. Figure from [3].

Polarized beams would also be implemented at the proposed electron-ion collider facility in China (EicC) [39], where the focus is stated to be on valence and sea-quark contributions to nucleon structure and effects of nucleus interactions. The first stage of the EicC will provide center-of-mass energies of $\sqrt{s} = 12 - 24$ GeV, while the second stage will function at energies of size $35 - 63$ GeV. These ranges permit values of x_p down to the scale 10^{-3} for $Q^2 = 5\,\mathrm{GeV}^2$.

5 Analysis

5.1 Monte Carlo integration

For the numerical integration, we use the GNU Scientific Library (GSL) which offers routines for multidimensional Monte Carlo integration [40]. These routines include algorithms such as VEGAS and MISER, adapted from the traditional Monte Carlo method, which use importance sampling and stratified sampling techniques. These algorithms, using a fixed amount of function calls, compute an estimate of a definite, multidimensional integral

$$I = \int_{x_l}^{x^u} \mathrm{d}x \int_{y_l}^{y^u} \mathrm{d}y \cdots f(x, y, \cdots). \tag{69}$$

The error estimate of a Monte Carlo integration result is given as a statistical estimate, calculated from the estimated variance of the mean. This means that it cannot be taken as a strict error bound, as it may be an underestimate of the actual error due to the nature of random sampling. The error estimate should decrease as $\sim 1/\sqrt{N}$, which means that to reduce the error tenfold one has to increase the number of sample points by around a hundredfold.

In this work, the VEGAS algorithm is used. This algorithm, formulated by G. Peter Lepage [41], is based on importance sampling. This means that the points which are sampled from the probability distribution are concentrated in the regions which account for the largest contribution to the integral. This differs from the usual Monte Carlo integration method, where integration points are uniformly distributed throughout all integration regions.

The general idea of the VEGAS algorithm as explained in Ref. [41] involves dividing the integration volume into hypercubes on a rectangular grid. In the first iteration, random points are uniformly distributed such that the average number of points in any hypercube region on the grid is the same as in any other region. Information gained in this first sampling is then used to define a new integration point density which adjusts the axes of the grid so as to concentrate the hypercubes in regions where the absolute value of the integrand is the largest. In this man-

ner, after each iteration the density of points is refined for the next iteration, thus gradually reducing the estimated error of the integration and obtaining a grid increasingly closer to the optimal one, where sample points are concentrated at those points where the integrand is largest.

In the GSL integration routine, if the Monte Carlo integral of function f is sampled with N points distributed according to a probability distribution described by a function g, an estimate $E_g(f;N) = E(f/g;N)$ for the integral is obtained. The general expression for the estimate is

$$E(f;N) = V\,\langle f\rangle = \frac{V}{N}\sum_{i}^{N} f(x_i), \tag{70}$$

where V is the volume of the integration region. The corresponding variance of the function over the integration region is $\mathrm{Var}_g(f;N) = \mathrm{Var}(f/g;N)$.

If the probability distribution is chosen to be $g = |f|/I(|f|)$, it can be shown that the variance vanishes and thus the error of the estimate will be zero. However, it is not possible in practice to sample from the exact distribution g of a function. Therefore, the algorithm aims to make an approximation of the distribution g. This is done by passing over the integration region multiple times while histogramming the function f, with each histogram used to define a sampling distibution for the next pass of the integration region. This will converge asymptotically towards the wanted distribution, just as the estimated grid mentioned earlier converges towards the optimally concentrated grid.

To minimize the number of histogram bins, the probability distribution is approximated by a separable function, $g(x_1, x_2, ...) = g(x_1)g(x_2)....$ This is equivalent to locating the peaks of the function from the projections of the integrand onto the coordinates axes. Since the efficiency of the algorithm depends on the validity of this assumption of a separable function, VEGAS is most efficient when the peaks of the integrand are well-localized. This corresponds to the optimal grid we wish to converge towards having its points concentrated at places where the integrand is largest. Thus, if the integrand can be written in a separable, or at least nearly separable form, the VEGAS integration efficiency will be higher.

The chi-squared per degree of freedom for the weighted estimate of the integral can be calculated using a function in GSL. If the value differs significantly from 1, it signifies that the values from different iterations are inconsistent, and the weighted error will be underestimated. Further iterations would thus be required for reliable

results to be obtained. In this work, a chi-squared value differing from 1 by a maximum of 0.25 was considered satisfactory.

5.2 Results

The jet transverse momentum spectra are calculated numerically for photon-proton scattering using Eqs. (58) and (59) and for photon-nucleus scattering using Eq. (68). Both scattering processes are studied at varying values of x_p and Q^2 and for photons both longitudinally and transversely polarized. At transverse momenta higher than about 6 GeV, the results begin to fluctuate and become unreliable, with large error bounds given by the Monte Carlo integration method. This type of fluctuation is somewhat expected at large momenta, as we are calculating a Fourier transform with solely discrete values of the function we are integrating over, that is, the dipole amplitude. While approaching increasingly large values of momentum, the results become more sensitive to small scale errors, for instance, the inaccuracies in the interpolation method as well as numerical fluctuation in the dipole amplitude values. Thus, the following figures have been cut off at a momentum $p_T \approx 6$ GeV.

In Fig. 8, we present the differential cross sections for photon-proton and photon-nucleus scattering for both photon polarizations, at two different values of momentum fraction x_p. The photon-proton spectrum in these figures has been scaled by the mass number of the nucleus and we would expect the two spectra to be quite near each other for each value of x_p, and it does appear that the general shape of the spectra are very similar for both scattering processes. Using these cross sections we can calculate nuclear suppression ratios R_{pA} (60).

We observe that for longitudinally polarized photons, the dependence of the cross section on p_T is stronger. This is because the splitting of the longitudinal photon into a $q\bar{q}$ dipole, see Eq. (28), is peaked at an even distribution of longitudinal momentum, $z_0 = z_1 = 0.5$, and therefore the dipole size $r \sim 1/Q$ at large Q^2. [42] For the transversely polarized photon, the structure of the wave function, Eq. (29), is different, with no such peak at any value of z. When either the quark q or the antiquark $\bar{q}$ carries a majority of the photon longitudinal momentum, the momentum fractions approach zero or one. This limit is not suppressed by the transverse photon wave function and thus, because the size of the dipole is a Fourier conjugate of the momentum exchange, large dipole sizes are not suppressed in the case of transverse polarization. As such, the transverse momentum (p_T) dependence of dipole size is weaker for transverse photons and therefore the initial p_T of quarks originating from

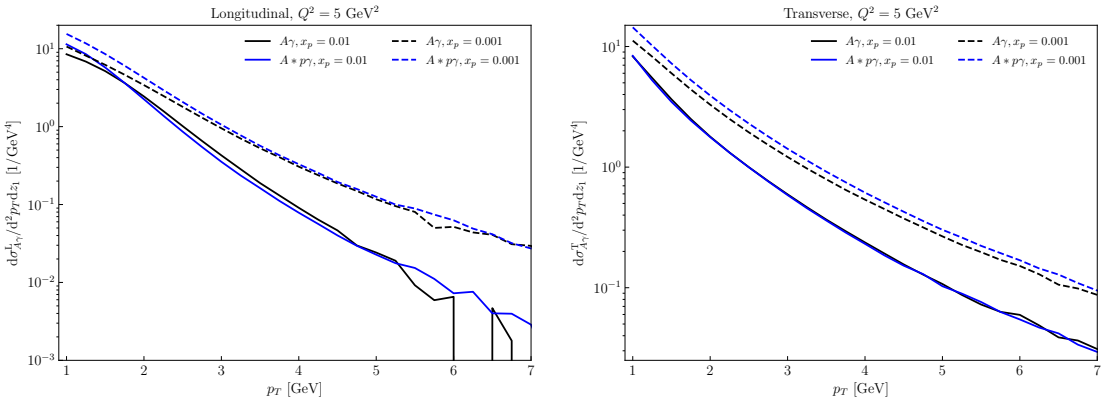

(a) (b)

Figure 8. Differential jet production cross section of (a) longitudinally and (b) transversely polarized photon-proton (blue) and photon-gold nucleus (black) scattering at $x_p = 0.01$ and $x_p = 0.001$, at $Q^2 = 5\,\mathrm{GeV}^2$ with the photon-proton spectrum scaled by the mass number of gold, $A = 197$. The sudden jump in the results at high p_T in (a) is due to fluctuations in the numerical calculation.

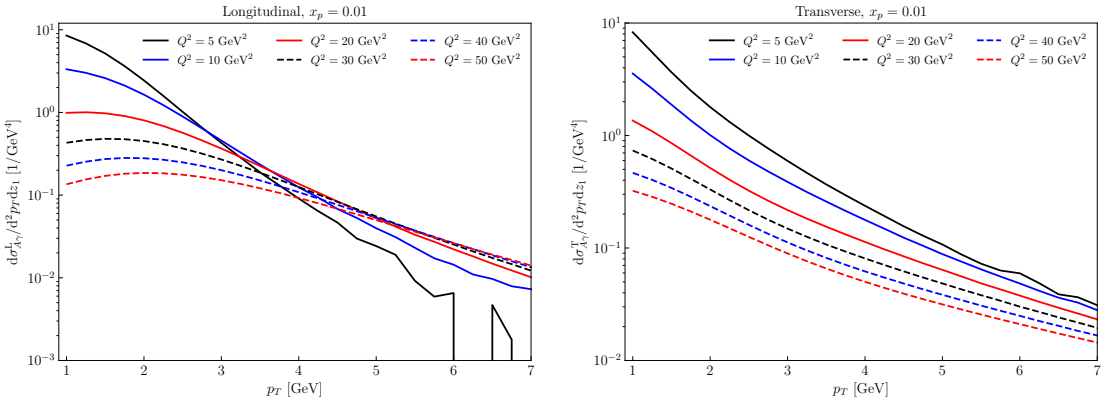

(a) (b)

Figure 9. Differential jet production cross section of (a) longitudinally and (b) transversely polarized photon-gold nucleus scattering at $x_p = 0.01$ for varying Q^2.

transverse photons is spread into a wider range than in the longitudinal case. It should be noted that, in this work, solely an equal division of photon longitudinal momentum between the quarks was considered. We showed in Sec. 2.2 that the momentum fraction z is related to rapidity, and therefore it is a variable which can indeed be measured experimentally.

The differential cross sections of jet production in both longitudinally and transversely polarized photon-gold nucleus scattering at $x_p = 0.01$ are shown in Fig. 9. For longitudinal photons, we notice that larger Q^2 values correspond to smaller cross sections at small p_T. However, at $p_T \gtrsim 4$ GeV, this is reversed, as larger Q^2 now corresponds to a larger value of the cross section. Similar behavior is also observed at smaller values of x_p, though they are not presented in the figure. For transversely polarized photons, as shown in Fig. 9b, larger values of Q^2 correspond to a smaller differential cross section at all values of p_T.

We know that, at large Q^2, the $q\bar{q}$ dipole which the photon splits into is small in size, especially so for longitudinal photons as discussed above. Because of the small size of the dipole, the relative transverse momentum between the quarks of the dipole is large. This can also be reasoned by considering a large-Q^2, zero-p_T photon, from which all energy must transfer into the dipole, which leads to a large transverse momentum for the quarks. If we now want to produce a small-p_T jet after scattering, which is effectively one particle at this p_T scale, this quark must receive a very large momentum kick from the target to diminish the total, large momentum already given to the dipole during the splitting from the photon. This is less probable than receiving a smaller momentum kick, which explains the notable size difference in cross sections at larger versus smaller Q^2 in the longitudinal case, as seen in Fig. 9a at $p_T < 3\,\mathrm{GeV}$.

We can also deduce this directly from the expression for the dipole amplitude $\mathcal{N}$. At small r, we can approximate the dipole to be linear, therefore letting us approximate $\mathcal{N}(\mathbf{r}) \sim \mathcal{N}(\mathbf{r}') \sim \mathbf{r}^2 Q_s^2$, which in momentum space is Q_s^2/Q^2. For the $\mathcal{N}(\mathbf{r}-\mathbf{r}')$ term, we can approximate $\mathcal{N}(|\mathbf{r}-\mathbf{r}'|) \sim \mathcal{N}(\sqrt{2}\mathbf{r}) \sim 2Q_s^2/Q^2$. Therefore, we see that for very large Q^2, $\mathcal{N}(\mathbf{r})+\mathcal{N}(\mathbf{r}')-\mathcal{N}(\mathbf{r}-\mathbf{r}') \to 0$, and this would explain the behavior at low values of $p_T \ll Q$, where the cross section is smaller for larger Q^2. This does not hold as strongly for transversely polarized photons, since the size distribution of dipoles is wider and does not peak as strongly at $r \sim 1/Q$. Therefore, we cannot see the same type of behavior in Fig. 9b as in the longitudinal photon case, Fig. 9a.

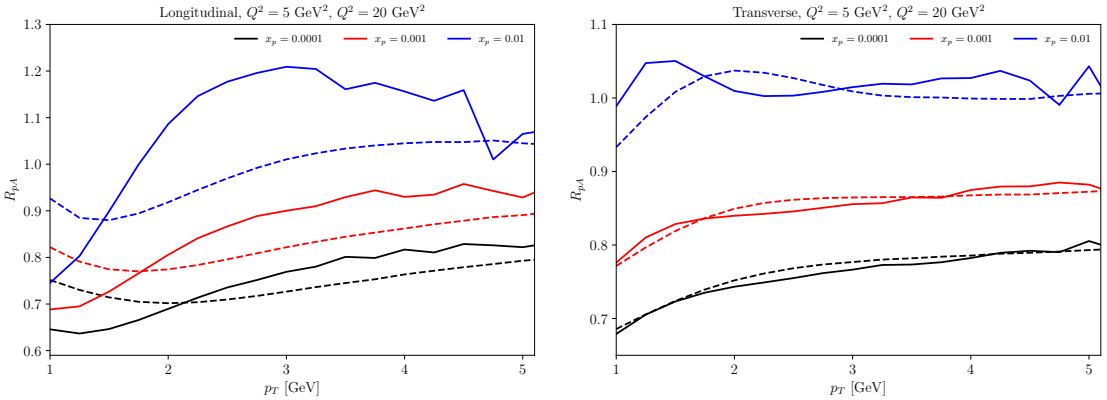

(a) (b)

Figure 10. Nuclear suppression ratio R_{pA} for (a) longitudinally polarized photons and (b) transversely polarized photons for varying values of x_p, at $Q^2 = 5$ GeV^2 (solid lines) and $Q^2 = 20$ GeV^2 (dashed lines).

The change in Fig. 9a at $p_T \gtrsim 4\,\text{GeV}$ to a larger Q^2 value corresponding to a larger cross section can be explained by the ϵ_f^2 term in the cross section Eqs. (58) and (59), originating from the photon wave function. Since ϵ_f^2 appears as a factor in both equations and is linearly dependent on Q^2, this term will dominate in large Q^2 interactions, but only once we are at high enough values of p_T so that the previously discussed difficulty in producing small-p_T jets at large Q^2 isn't dominant. Thus, the cross section increases with increasing Q^2 after $4\,\text{GeV}$.

In Fig. 10, the ratios R_{pA} in the case of longitudinal and transverse photon polarizations are presented. We note as a general trend that as x_p decreases the nuclear suppression ratio R_{pA} decreases as well, which means that suppression in photon-nucleus interactions increases with decreasing momentum fraction x_p. This is as expected, since with decreasing x_p the saturation scale Q_s of the nucleus grows and, as a result, saturation effects are more pronounced. From these figures, we see that especially the behavior of R_{pA} at small values of p_T is different for the two polarizations. In the longitudinal case, Fig. 10a, there is a noticable dip in the ratio at the lower end of p_T which does not appear in the transverse case. Furthermore, in the transverse case, Fig. 10b, at $x_p = 0.01$ there appears to be a peak in R_{pA} at around the same value. In the total, polarization-summed R_{pA}, shown in Fig. 11, we see that neither of these behaviors is clearly visible.

The linearization discussion for the dipole amplitudes can also be used to explain R_{pA} decreasing with p_T in the small momentum range in the longitudinal case. The

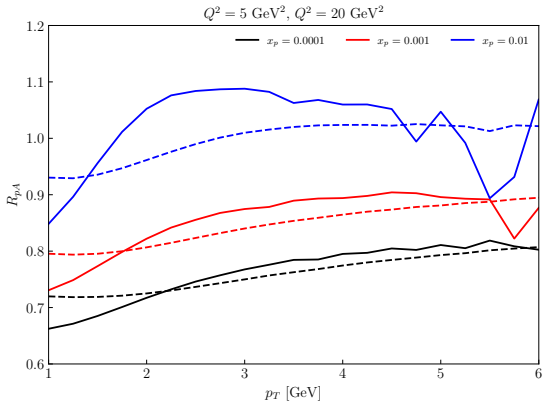

Figure 11. Total nuclear suppression ratio R_{pA} at $Q^2 = 5$ GeV^2 (solid lines) and $Q^2 = 20$ GeV^2 (dashed lines) for varying values of x_p. Contributions of both photon polarizations have been summed.

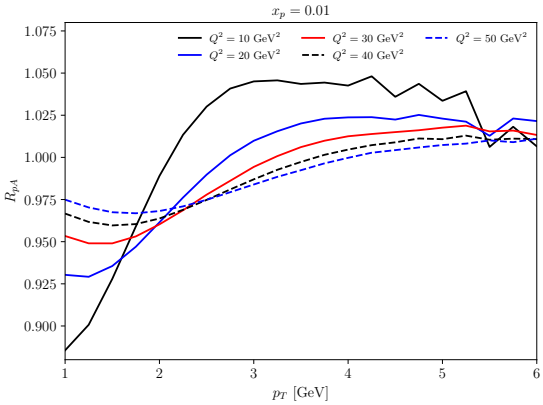

Figure 12. Total nuclear suppression ratio R_{pA} at $x_p = 0.01$ for varying values of Q^2.

linearization of the amplitudes works better for proton-photon processes than for the scattering with the nucleus. Only at the dilute limit does the sum of dipole amplitudes in Eq. (57) approach zero. Nonlinearities in the dipole amplitude $\mathcal{N}$ prevent this, and since the nuclear amplitude is more nonlinear than that of the proton, the sum of the three amplitude terms goes to zero slower in nucleus interactions than in those involving protons. This is why in Fig. 10a we see that R_{pA} first decreases with increasing p_T before increasing again.

The behavior of R_{pA} with varying Q^2 seen in Fig. 12 is quite interesting, since at $p_T \lesssim 2$ GeV the suppression is stronger for smaller Q^2, while at momenta above this, the processes at larger Q^2 are more suppressed those at smaller Q^2. This can be explained in a similar manner as the case of small-p_T behavior in Fig. 9a. The nucleus has a larger saturation scale, Q_s, than the proton when probed at the same x_p and, in our framework, most of the gluons in the target hadron have values of transverse momentum of the scale Q_s. Again, at large values of Q^2, the quarks have a significantly large transverse momentum given to them by the virtual photon. To obtain a small-p_T jet as a final product from the interaction of a high-p_T quark and the target hadron, the hadron must give a large kick to the quark in order to slow it down. The size scale of the kick is relative to the target's saturation scale Q_s, so the kick from a nucleus is generally stronger. Therefore, as it is easier for the nucleus to give a large enough kick to obtain a small-p_T jet than it is for a proton to do the

same, this results in the growth of nuclear suppression ratio R_{pA} at small p_T, and the effect is more significant the larger the value of Q^2, as shown in Fig. 12.

In Fig. 12, we see that the nuclear suppression factor actually reaches values above unity at lower values of Q^2 in the intermediate p_T area. This means that instead of suppression the results display an enhancement of the photon-nucleus interactions. This type of effect in which the suppression ratio exceeds unity is referred to as the Cronin effect [43]. As stated previously, the transverse momentum that a quark obtains as it scatters from the color field of a nucleus is typically larger than in the case of it scattering from a proton. Before interaction, the transverse momentum of the quark is of the order Q. The kick given by the target is likely to be larger from the nucleus than from the proton, and it is therefore more probable that a jet or particle in this p_T range is produced from the nucleus. This raises the nuclear suppression ratio above unity at intermediate p_T values. We notice that the peak shifts to higher p_T as Q^2 increases. The Cronin effect has been observed in multiple experiments, first at lower fixed target energies [43] and later on at RHIC d-Au collision experiments [44, 45].

At larger values of p_T, the nuclear suppression ratio R_{pA} asymptotically approaches unity, as is expected. As we head towards larger values of transverse momentum, the transverse separation r becomes increasingly smaller. With decreasing r, the coupling becomes weaker, and as the quark and antiquark together becomes color neutral when $r \to 0$, they are no longer affected by the strong interaction. Therefore, the nonlinear effects in the nucleus diminish. This behavior continues with increasing p_T until the nonlinear effects are effectively nonexistent and the nuclear suppression effect is no longer noticeable, and so at sufficiently large p_T, $R_{pA} = 1$. Also, it is to be noted that the dipole amplitudes used in this work have been calculated using the assumption that at high enough p_T we eventually must have $R_{pA} = 1$. [34]

At smaller values of x_p, the Cronin effect is diminished by the BK evolution equation. [46] This can be observed in Fig. 11 for those results with x_p smaller than 0.01. This diminishment of initial enhancement is mostly due to linear BFKL dynamics, which are included in the BK evolution equation. For small enough x_p, the Cronin type enhancement effectively dissappears completely. [46] The reduction, yet not complete dissappearance of the Cronin effect in forward rapidity deuteron-gold collisions at RHIC was shown in Ref. [46] to be consistent with the results given by the BK evolution equation, while the complete dissappearance of the effect for

proton-nucleus collisions at the LHC was also predicted. This has been shown to, most likely, be the case, as experiments at the LHC have indicated a very small magnitude of the Cronin effect, with the data also consistent with a case of zero enhancement once systematic uncertainties are taken into account. [47]

Since in our calculations we have only taken into account BK evolution, which is logarithmic in $1/x_p$, and not DGLAP evolution, which is logarithmic in Q^2, we want to have $\ln(Q^2) \ll \ln(1/x_p)$ to ensure that BK evolution is the dominant one. This is ensured by the choice to study parameter dependence at values $10^{-4} \leq x_p \leq 10^{-2}$ and 5 GeV$^2 \leq Q^2 \leq 50$ GeV^2. Ideally, we would have both evolution equations as the basis of our equations, but their combination is not yet feasible.

As mentioned earlier, we consider collisions in which the photon splits into a quark and antiquark of equal momentum, $z_0 = z_1 = 0.5$. If we were to integrate over the momentum fractions z_i, we would be considering contributions from a widely spread spectrum of dipole sizes at very small and large z_i, especially so for transversely polarized photons. This means that we would take into account also those contributions from areas with very large dipole sizes, which are consequently areas with very small transverse momenta. Without a limit on the dipole size, this could cause potential problems related to confinement scale physics. This problem has been solved in some cases by setting a maximum value for the dipole size by introducing an effective gluon mass to regulate the dipole size. [48]

5.3 Model dependence

The results shown in Sec. 5.2 have all been calculated in the so-called MV^e parametrization for the nonperturbative input of the BK evolution equation, as described in Sec. 2.3. In order to see if our results are sensitive to the chosen parametrization model, we repeat similar calculations in the pure MV model to compare the two. The difference between the two parametrizations is in the initial condition for the dipole amplitude (22): in the MV model, $e_c \equiv 1$, whereas in the MV^e model, e_c is kept as a free parameter. This affects other parameters as well, which have been obtained from fits to HERA reduced cross section data [34] and are listed in Table 1. Both models are thus compatible with the experimental data obtained from HERA.

In Fig. 13, the nuclear suppression ratio R_{pA} is shown for both MV and MV^e models at two different values of x_p. We see that there is a very small difference

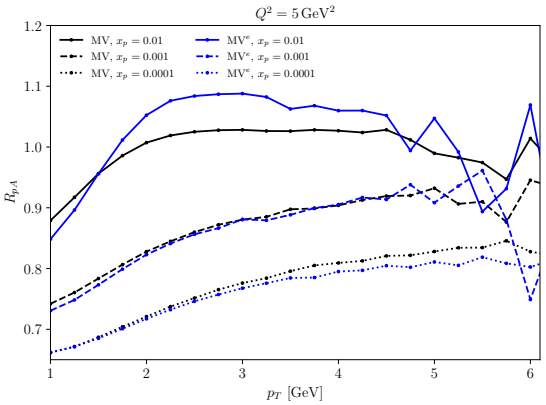

Figure 13. Nuclear suppression ratio R_{pA} in MV^e (blue) and MV (black) models for varying values of x_p, for $Q^2 = 5$ GeV^2. The fluctuation of the data at larger p_T is due to uncertainty of our numerical calculation.

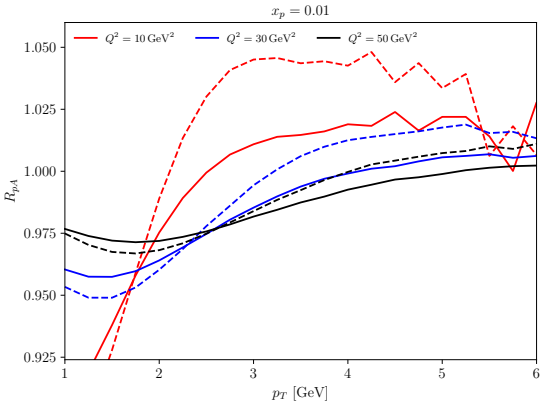

Figure 14. Nuclear suppression ratio R_{pA} in MV (solid lines) and MV^e (dashed lines) models for varying values of Q^2, for $x_p = 0.01$.

between the ratios at lower x_p, while at $x_p = 0.01$ the ratios given by the two models do differ somewhat. The initial conditions for the MV model were given at $x_p = 0.01$, and the BK evolution tells how the results change with decreasing x_p. Therefore, the larger difference between the models at $x_p = 0.01$ might be due to the initial conditions, and at smaller x_p, the BK evolution seems to diminish the difference. At values of $p_T > 5$ GeV, calculations with both models give fluctuating and therefore quite unreliable results.

In Fig. 14, the ratios R_{pA} given by both models are shown for varying values of Q^2 at $x_p = 0.01$. At the larger values of Q^2, the two models seem to give very similar results. However, at $Q^2 = 10$ GeV^2, there is a slight difference in the results, and, as shown in Fig. 13, an even bigger difference of nearly 10% is seen at $Q^2 = 5$ GeV^2. This suggests that there is some dependence of the results on the model chosen, and with the models we have used, this is seen especially at low Q^2 and at values of x_p near the initial condition.

Results from upcoming experiments on jet production will provide complementary knowledge on the choice of a suitable theoretical model, as data from structure function measurements has been used for the parametrization fitting and does not present such differences between the models. Once experimental results are obtained, one can compare them to both the MV and MV^e predictions as well as results calculated using other models, and then consider which of them corresponds

to the experimental results the best.

5.4 Relation to other approaches

In Ref. [49], predictions are presented for single inclusive jet photoproduction using the color dipole formalism, the same framework used in our work, in p-p and p-Pb collisions. The major difference between our subjects of study is that Ref. [49] considers real photons generated by the hadron, while in our work we consider virtual photons emitted by electrons. The study in Ref. [49] considers ultraperipheral collisions in the LHC, where photon-induced interactions become the dominant ones [50]. This is because, in these events, the interacting hadrons are far from each other and thus the range of strong interaction is not enough to counter the photon-induced interactions. Therefore, the dominant process is one where the ultrarelativistic hadrons act as a source of real photons. The photon then splits into a dipole and scatters off the other hadron, similarly as in our work.

Inclusive and diffractive dijet production cross sections in e-p and e-A collisions at the EIC, using the CGC theory, have been computed in Ref. [51]. These results suggest that a regime of mean dijet transverse momentum of the size scale $\sim Q_s$ at the EIC might give interesting results in dijet production studies, as the results appear to depend on the target's properties, such as parton structure and saturation effects. The authors also state that saturation effects are significant in the kinematic regime considered, which is shown by studying the nuclear modification of the ratio of diffractive and inclusive events.

In Ref. [52], similarly, dijet production at the future EIC is considered, the main focus being an assessment of the feasability of measuring gluon distributions through dijet production. One of the findings of the study is that a more realistic modelling of the impact parameter dependence of the target nucleus thickness would be useful in improving the analysis.

In Ref. [53], the dipole picture is used to study the effects of gluon saturation in the nucleus on the cross section of SIDIS in e-A collisions at small Bjorken x. This is quite similar to our work, however, the study considers an uneven longitudinal momentum division between the dipole quarks, while in our work, we consider an even distribution of momentum. The study suggests that if a hadron or jet with a large fraction z of the virtual photon momentum is tagged, then working in the limit $z(1-z)Q^2 \ll Q_s^2$ might present new phenomena signalling saturation in the SIDIS

cross section. A Cronin peak is also seen in the study at this limit at moderate values of x, and when x decreases, the peak dissappears and is replaced by suppression, as is the case also in our work.

6 Conclusions

We have performed a study of jet production in semi-inclusive deep inelastic scattering using the dipole model formalism at varying values of momentum fraction x_p and photon virtuality Q^2. In our calculations, the running coupling BK evolution of the dipole scattering amplitude takes nonlinear, saturation regime effects into account, with the MV model as the input. By comparing scattering between a photon and a proton to that between a photon and a nucleus, we have been able to present effects of gluon saturation within the nucleus on jet production.

The nuclear suppression ratio R_{pA} gives information on suppression effects in nuclei, therefore, we have studied these ratios in the case of jet production. Our findings have shown that suppression effects are visible at lower values of transverse jet momentum p_T, while at higher p_T, these effects tend to vanish as the ratio approaches unity. The dipole amplitude model used in this work is based on the assumption that the amplitudes approach unity at large p_T, and so the chosen model has an effect on the high-p_T behavior of the ratio.

By studying R_{pA}, we have found the expected result that suppression in photon-nucleus interactions increases as x_p decreases. While suppression is seen in the lower values of p_T, Cronin enhancement is observed at intermediate p_T values when x_p is large enough, around $x_p \approx 10^{-2}$. It is expected that at smaller values of x_p, that is, at higher energies, the Cronin effect will diminish by the BK evolution equation. This diminishing behavior at small x_p has been observed in our work, and it has also been previously shown that, at LHC energies, the Cronin effect is nearly or even completely dissipated. We expect to see a Cronin peak as well as its dissipation in the EIC at the anticipated kinematic range of experiments.

A difference between the two polarizations of the photons was seen while comparing their corresponding jet production cross sections. We have discussed how the dependence of the cross sections on transverse momentum is stronger for longitudinally polarized photons than for transversely polarized photons. This serves as an explanation for why, especially at low p_T, the behavior of the cross sections and ratios R_{pA} differs between the photon polarizations.

We have compared the differences between two parametrizations for the initial conditions of perturbative small-x evolution used in calculating the dipole amplitudes, the MV and MV^e models, of which the latter was used in all other calculations in the work. Other parametrizations for the MV model exist as well, although they were not considered here. A slight difference was found between the R_{pA} results given by the different parametrization models at low Q^2 and high x_p. At $x_p = 0.01$ and $Q^2 = 5$ GeV^2, the ratio R_{pA} differs the most, by nearly 10%. The initial conditions for the models are in fact given at the point $x_p = 0.01$, so this might be a reason why the models differ the most at this exact x_p. The BK evolution washes out the effect of the initial condition as we head towards smaller values of x_p. The study of jet production offers us important, complementary information on nuclei and protons and, according to the results of our work, jet production data from the future EIC can be used to constrain the dipole amplitude towards a model that seems to suit the data best.

There exists some uncertainty in our numerical calculations which is especially notable at values of p_T higher than 6 GeV. This could be improved upon by attempting other integration methods. The fractions of longitudinal momenta z_i were set equal to one another in this work. Another option of study would be to consider the whole range of momentum fractions by integrating over these variables, however, the resulting very large dipole sizes may have to be regulated in some way to prevent problems arising from confinement.

References

[1] **H1, ZEUS** collaboration, H. Abramowicz *et. al.*, *Combination of measurements of inclusive deep inelastic $e^{\pm}p$ scattering cross sections and QCD analysis of HERA data*, *Eur. Phys. J. C* **75** (2015) no. 12 580 [arXiv:1506.06042 [hep-ex]].

[2] A. Accardi, J. L. Albacete, M. Anselmino, N. Armesto *et. al.*, *Electron Ion Collider: The Next QCD Frontier - Understanding the glue that binds us all*, *European Physical Journal A* **52** (2016) no. 9 .

[3] **LHeC, FCC-he Study Group** collaboration, P. Agostini *et. al.*, *The Large Hadron-Electron Collider at the HL-LHC*, arXiv:2007.14491 [hep-ex].

[4] T. Altinoluk, N. Armesto, G. Beuf and A. H. Rezaeian, *Diffractive Dijet Production in Deep Inelastic Scattering and Photon-Hadron Collisions in the Color Glass Condensate*, *Phys. Lett. B* **758** (2016) 373 [arXiv:1511.07452 [hep-ph]].

[5] Y. V. Kovchegov and E. Levin, *Quantum Chromodynamics at High Energy*. Cambridge University Press, 2012.

[6] R. K. Ellis, B. R. Webber and W. J. Stirling, *QCD and Collider Physics*. No. Vol. 8 in Cambridge Monographs on Particle Physics, Nuclear Physics, and Cosmology. Cambridge University Press, 1996.

[7] B. R. Martin and G. Shaw, *Particle physics*. John Wiley, Chichester, 4th ed., 2017.

[8] V. N. Gribov and L. N. Lipatov, *Deep inelastic e p scattering in perturbation theory*, *Sov. J. Nucl. Phys.* **15** (1972) 438.

[9] V. N. Gribov and L. N. Lipatov, *e+ e- pair annihilation and deep inelastic e p scattering in perturbation theory*, *Sov. J. Nucl. Phys.* **15** (1972) 675.

[10] G. Altarelli and G. Parisi, *Asymptotic Freedom in Parton Language*, *Nucl. Phys. B* **126** (1977) 298.

[11] Y. L. Dokshitzer, *Calculation of the Structure Functions for Deep Inelastic Scattering and e+ e- Annihilation by Perturbation Theory in Quantum Chromodynamics.*, *Sov. Phys. JETP* **46** (1977) 641.

[12] E. A. Kuraev, L. N. Lipatov and V. S. Fadin, *The Pomeranchuk Singularity in Nonabelian Gauge Theories*, *Sov. Phys. JETP* **45** (1977) 199.

[13] I. I. Balitsky and L. N. Lipatov, *The Pomeranchuk Singularity in Quantum Chromodynamics*, *Sov. J. Nucl. Phys.* **28** (1978) 822.

[14] F. Carvalho, F. O. Duraes, V. P. Goncalves and F. S. Navarra, *Gluon saturation and the Froissart bound: A Simple approach*, *Mod. Phys. Lett. A* **23** (2008) 2847 [arXiv:0705.1842 [hep-ph]].

[15] E. Iancu, A. Leonidov and L. D. McLerran, *Nonlinear gluon evolution in the color glass condensate. 1.*, *Nucl. Phys. A* **692** (2001) 583 [arXiv:hep-ph/0011241].

[16] L. D. McLerran and R. Venugopalan, *Computing quark and gluon distribution functions for very large nuclei*, *Phys. Rev. D* **49** (1994) 2233 [arXiv:hep-ph/9309289].

[17] L. D. McLerran and R. Venugopalan, *Gluon distribution functions for very large nuclei at small transverse momentum*, *Phys. Rev. D* **49** (1994) 3352 [arXiv:hep-ph/9311205].

[18] L. D. McLerran and R. Venugopalan, *Green's functions in the color field of a large nucleus*, *Phys. Rev. D* **50** (1994) 2225 [arXiv:hep-ph/9402335].

[19] G. Beuf, *NLO corrections for the dipole factorization of DIS structure functions at low x*, *Phys. Rev. D* **85** (2012) 034039 [arXiv:1112.4501 [hep-ph]].

[20] K. G. Wilson, *Confinement of Quarks*, *Phys. Rev. D* **10** (1974) 2445.

[21] I. Balitsky, *High-energy QCD and Wilson lines*, arXiv:hep-ph/0101042.

[22] M. E. Peskin and D. V. Schroeder, *An Introduction to Quantum Field Theory.* Perseus Books, Reading, USA, 1995.

[23] I. Balitsky, *Operator expansion for high-energy scattering*, *Nucl. Phys. B* **463** (1996) 99 [arXiv:hep-ph/9509348].

[24] Y. V. Kovchegov, *Small-x F_2 structure function of a nucleus including multiple pomeron exchanges*, *Phys. Rev. D* **60** (1999) 034008 [arXiv:hep-ph/9901281].

[25] E. Iancu, A. Leonidov and L. D. McLerran, *The Renormalization group equation for the color glass condensate*, *Phys. Lett. B* **510** (2001) 133 [arXiv:hep-ph/0102009].

[26] J. Jalilian-Marian, A. Kovner, A. Leonidov and H. Weigert, *The Wilson renormalization group for low x physics: Towards the high density regime*, *Phys. Rev. D* **59** (1998) 014014 [arXiv:hep-ph/9706377].

[27] J. Jalilian-Marian, A. Kovner, A. Leonidov and H. Weigert, *Unitarization of gluon distribution in the doubly logarithmic regime at high density*, *Phys. Rev. D* **59** (1999) 034007 [arXiv:hep-ph/9807462]. [Erratum: Phys.Rev.D 59, 099903 (1999)].

[28] J. Jalilian-Marian, A. Kovner and H. Weigert, *The Wilson renormalization group for low x physics: Gluon evolution at finite parton density*, *Phys. Rev. D* **59** (1998) 014015 [arXiv:hep-ph/9709432].

[29] J. L. Albacete, N. Armesto, J. G. Milhano, P. Quiroga-Arias and C. A. Salgado, *AAMQS: A non-linear QCD analysis of new HERA data at small-x including heavy quarks*, *Eur. Phys. J. C* **71** (2011) 1705 [arXiv:1012.4408 [hep-ph]].

[30] I. Balitsky, *Quark contribution to the small-x evolution of color dipole*, *Phys. Rev. D* **75** (2007) 014001 [arXiv:hep-ph/0609105].

[31] Y. V. Kovchegov and H. Weigert, *Triumvirate of Running Couplings in Small-x Evolution*, *Nucl. Phys. A* **784** (2007) 188 [arXiv:hep-ph/0609090].

[32] J. L. Albacete and C. Marquet, *Single Inclusive Hadron Production at RHIC and the LHC from the Color Glass Condensate*, *Phys. Lett. B* **687** (2010) 174 [arXiv:1001.1378 [hep-ph]].

[33] J. L. Albacete and C. Marquet, *Azimuthal correlations of forward di-hadrons in d+Au collisions at RHIC in the Color Glass Condensate*, *Phys. Rev. Lett.* **105** (2010) 162301 [arXiv:1005.4065 [hep-ph]].

[34] T. Lappi and H. Mäntysaari, *Single inclusive particle production at high energy from HERA data to proton-nucleus collisions*, *Phys. Rev. D* **88** (2013) 114020 [arXiv:1309.6963 [hep-ph]].

[35] L. D. McLerran and R. Venugopalan, *Computing quark and gluon distribution functions for very large nuclei*, *Phys. Rev. D* **49** (1994) 2233 [arXiv:hep-ph/9309289].

[36] Mäntysaari, Heikki, "rcbkdipole." https://github.com/hejajama/rcbkdipole.

[37] Brookhaven National Laboratory, "Electron Ion Collider." https://www.flickr.com/photos/brookhavenlab/49922694018/in/album-72157714316624996/, 2020. Accessed: 19.3.2021.

[38] **FCC** collaboration, A. Abada *et. al.*, *HE-LHC: The High-Energy Large Hadron Collider: Future Circular Collider Conceptual Design Report Volume 4*, *Eur. Phys. J. ST* **228** (2019) no. 5 1109.

[39] X. Chen, *A Plan for Electron Ion Collider in China*, *PoS* **DIS2018** (2018) 170 [arXiv:1809.00448 [nucl-ex]].

[40] GSL Team, "Monte Carlo Integration." https://www.gnu.org/software/gsl/doc/html/montecarlo.html. Accessed 22.05.2020.

[41] G. P. Lepage, *VEGAS - an adaptive multi-dimensional integration program*, Mar, 1980. https://cds.cern.ch/record/123074.

[42] H. G. Dosch, T. Gousset, G. Kulzinger and H. J. Pirner, *Vector meson leptoproduction and nonperturbative gluon fluctuations in QCD*, *Phys. Rev. D* **55** (1997) 2602 [arXiv:hep-ph/9608203].

[43] J. Cronin, H. J. Frisch, M. Shochet, J. Boymond, R. Mermod, P. Piroue and R. L. Sumner, *Production of hadrons with large transverse momentum at* 200*,* 300*, and* 400 *GeV*, *Phys. Rev. D* **11** (1975) 3105.

[44] **BRAHMS** collaboration, I. Arsene *et. al.*, *On the evolution of the nuclear modification factors with rapidity and centrality in d + Au collisions at* $\sqrt{s_{NN}} = 200$ *GeV*, *Phys. Rev. Lett.* **93** (2004) 242303 [arXiv:nucl-ex/0403005].

[45] **PHENIX** collaboration, S. Adler *et. al.*, *Absence of suppression in particle production at large transverse momentum in* $\sqrt{s_{NN}} = 200$ *GeV* $d + Au$ *collisions*, *Phys. Rev. Lett.* **91** (2003) 072303 [arXiv:nucl-ex/0306021].

[46] J. L. Albacete, N. Armesto, A. Kovner, C. A. Salgado and U. A. Wiedemann, *Energy dependence of the Cronin effect from nonlinear QCD evolution*, *Phys. Rev. Lett.* **92** (2004) 082001 [arXiv:hep-ph/0307179].

[47] **ALICE** collaboration, B. Abelev *et. al.*, *Transverse momentum distribution and nuclear modification factor of charged particles in p-Pb collisions at* $\sqrt{s_{NN}} = 5.02$ *TeV*, *Phys. Rev. Lett.* **110** (2013) no. 8 082302 [arXiv:1210.4520 [nucl-ex]].

[48] J. Berger and A. M. Staśto, *Small x nonlinear evolution with impact parameter and the structure function data*, *Phys. Rev. D* **84** (2011) 094022 [arXiv:1106.5740 [hep-ph]].

[49] V. P. Gonçalves, G. Sampaio dos Santos and C. R. Sena, *Single inclusive jet photoproduction at very forward rapidities in pp and pPb collisions at the LHC*, *Eur. Phys. J. C* **80** (2020) no. 6 521 [arXiv:1911.00345 [hep-ph]].

[50] C. A. Bertulani, S. R. Klein and J. Nystrand, *Physics of ultra-peripheral nuclear collisions*, *Ann. Rev. Nucl. Part. Sci.* **55** (2005) 271 [arXiv:nucl-ex/0502005].

[51] H. Mäntysaari, N. Mueller, F. Salazar and B. Schenke, *Multigluon Correlations and Evidence of Saturation from Dijet Measurements at an Electron-Ion Collider*, *Phys. Rev. Lett.* **124** (2020) no. 11 112301 [arXiv:1912.05586 [nucl-th]].

[52] A. Dumitru, V. Skokov and T. Ullrich, *Measuring the Weizsäcker-Williams distribution of linearly polarized gluons at an electron-ion collider through dijet azimuthal asymmetries*, *Phys. Rev. C* **99** (2019) no. 1 015204 [arXiv:1809.02615 [hep-ph]].

[53] E. Iancu, A. H. Mueller, D. N. Triantafyllopoulos and S. Y. Wei, *Saturation effects in SIDIS at very forward rapidities*, arXiv:2012.08562 [hep-ph].